Film drainage and coalescence between deformable drops and bubbles†

Derek Y. C. Chan,‡*[abc] Evert Klaseboer[b] and Rogerio Manica[b]

Received 13th August 2010, Accepted 30th October 2010
DOI: 10.1039/c0sm00812e

The interaction between deformable drops or bubbles encompasses a number of distinguishing characteristics not present in the interaction between solid bodies. The drops can entrap a thin liquid film of the continuous phase that can lead to a stable film or coalescence. But before leading to either of these outcomes, the film must drain under the influence of an external driving force. This drainage process exhibits all the characteristic features of dynamic interactions between soft materials. For example, the spatial and temporal variations of forces and geometric deformations, arising from hydrodynamic flow, surface forces and variations in material properties, are all inextricably interconnected. Recent measurements of time-varying deformations and forces between interacting drops and bubbles confirmed that dynamic forces and geometric deformations are coupled and provide the key to understand novel phenomena such as the "wimple" in mechanically perturbed films. The counter-intuitive phenomenon of coalescence triggered by separating proximal drops or bubbles can also be elucidated using the same theoretical framework. One approach to modelling such systems is to use a fluid mechanics formulation of two-phase flow for which a number of parametric numerical studies have been made. Another popular approach focuses on describing the thin film between the interacting drops or bubbles with a flat film model upon which a phenomenological film drainage and rupture mechanism has been developed. While both models have a similar genesis, their predictions of the fate of the draining film are quite different. Furthermore, there have been few quantitative comparisons between results obtained from many different experimental approaches with either theory. One reason for this is perhaps due to difficulties in matching experimental parameters to model conditions. A direct attempt to model dynamic behaviour in many experimental studies is challenging as the model needs to be able to describe phenomena spanning six orders of magnitude in length scales. However, with the recent availability of accurate experimental studies concerning dynamic interaction between drops and bubbles that use very different, but complementary approaches, it is timely to conduct a critical review to compare such results with long-accepted paradigms of film stability and coalescence. This topic involves the coupling of behaviour on the millimetre–micrometre scale familiar to readers with an engineering and fluid mechanics background to phenomena on the micrometre–nanometre scale that is the domain of the interfacial science and nanotechnology community.

1. Introduction

1.1 Background

A feature that is central to understanding interactions involving soft materials is the interdependence between variations in geometric deformations and the strength of the interaction. For rigid bodies, only the unchanging geometry around the interaction zone between surfaces in close proximity needs to be specified in order to determine the interaction force. Soft bodies, on the other hand, can change shape in response to local variations of the interaction force so that the total force and the corresponding geometric variations must satisfy a mechanical equation of state that characterises deformations. If the deformable material is incompressible, then local shape variations can give rise to long-range effects. For an extendable spring, its length is related to the tensile or compressive force acting upon it. Generalising this concept to soft materials, knowledge of the distribution of forces acting on a deformable body is equivalent to knowing the deformed shape, provided one has the material equation of state that relates forces to deformations—the analogue of Hooke's Law for springs.

However, this coupling between forces and geometries can extend over length scales of many orders of magnitude. For example, the interaction between millimetre size drops or bubbles across films of nanometre thickness can cause deformations extending over tens to hundreds of micrometres. The incompressibility of drops and to a good approximation, bubbles,

[a]*Department of Mathematics & Statistics, Particulate Fluids Processing Centre, The University of Melbourne, Parkville, Victoria, 3010, Australia. E-mail: D.Chan@unimelb.edu.au; Fax: +61 3 8344 4599; Tel: +61 3 8344 5556*
[b]*Institute of High Performance Computing, 1 Fusionopolis Way, 138632, Singapore. E-mail: evert@ihpc.a-star.edu.sg; manicar@ihpc.a-star.edu.sg; Fax: +65 6463 0200; Tel: +65 6419 1111*
[c]*Department of Mathematics, National University of Singapore, 117543, Singapore. E-mail: D.Chan@unimelb.edu.au*

† Electronic supplementary information (ESI) available: Animations of the deformation of drops and bubbles during interaction, videos of symmetry breaking events during coalescence and an example of Marangoni flow. See DOI: 10.1039/c0sm00812e

‡ D.Y.C.C. is an Adjunct Professor at the National University of Singapore and a Visiting Scientist at the Institute of High Performance Computing.

means that small changes on the scale of the size of drops or bubbles can have significant effects on the scale of thin films.[1]

The drainage or thinning process of the liquid film between interacting drops or bubbles is time dependent so dynamic effects on different length scales will need to be measured with appropriate precision to facilitate quantitative analysis—an experimental challenge that is often not easy to meet.[2]

'*The difficulties encountered in the design and operation of industrial equipment in which coalescence occurs is partly due to a lack of knowledge of coalescence*'. Though this statement was written almost 40 years ago,[3] it is still true to a large extent today. Since that time, there have been many attempts to measure the dynamics of film drainage and coalescence of drops and bubbles, but few succeeded to measure the time-dependent variations in forces and deformations in sufficient detail and precision on different length scales for quantitative analysis. Consequently, phenomenological models have been proposed and accepted without independent critique.

The past decade witnessed the increasing availability of high precision measurements of temporal and spatial information associated with film drainage and coalescence of drops and bubbles using a variety of experimental techniques. In addition, direct measurements of the time dependent force between drops, bubbles and solids in relative motion in the atomic force microscope have also become possible. This body of data can now be subjected to quantitative comparisons using models that share a common theoretical underpinning. By undertaking such a comparison in this review, we hope to bridge the existing gap between experiment and theory and to offer a critique of the state of commonly accepted notions of film drainage and coalescence of drops and bubbles.

1.2 Scope

This review will focus on time-dependent interfacial deformation, interaction force and film drainage phenomena associated with drop or bubble sizes on the millimetre to micrometre scale. This size range is of particular relevance to material processing applications and for which the effects of gravity on the drop or bubble shapes are negligible. The regime of film thickness can be down to nanometres so that both colloidal forces and hydrodynamic interactions need to be considered. We therefore concentrate on a theoretical model that includes all these elements in a consistent manner. Experimental studies that we have chosen to highlight are those for which sufficient details have been reported to permit quantitative comparison with theory. A distinguishing feature of this review is that we use a common theoretical framework to interpret and compare experimental results obtained from very different techniques that provides complementary information about dynamic interactions between drops and bubbles. Such an approach offers clear insight into the key physical elements that are central to this complex problem.

We have two readership constituencies in mind: those with an engineering and continuum mechanics background who are familiar with material processing on the millimetre to micrometre scale and those from the interfacial science and nanotechnology community whose interests are in phenomena on the micrometre to nanometre scale. Therefore as background material, we first provide a summary of different kinds of experimental methods: those based on techniques that measure the spatial and temporal evolution of the drainage and deformation of thin films formed

Derek Y. C Chan

Derek Chan received his PhD in Applied Mathematics from the Australian National University and BSc (Hons) in Physics from the University of New South Wales, where he failed to complete a degree in Electrical Engineering. He has worked at Unilever Research, Port Sunlight and Bristol University prior to joining the University of Melbourne in the last century. When he is not on the tennis court, he enjoys solving theoretical problems in interfacial science, fluid mechanics, statistical mechanics and surface chemistry in collaborations with experimental colleagues in the Particulate Fluids Processing Centre.

Evert Klaseboer

Evert Klaseboer studied Applied Physics (Twente University, The Netherlands). After a brief period of farming, he completed his PhD in Process Engineering at the Institut National Polytechnique de Toulouse (France) on the subject "Drainage of thin films between two drops with Marangoni effects". He joined the Institute of High Performance Computing in Singapore in 2000. His research interests are bubble and drop dynamics ranging from underwater explosions to drop coalescence. When he is not busy thinking about the physics of fluids, he hunts for rare stamps to add to his extensive collection.

Rogerio Manica

Rogerio Manica received his Bachelor and Masters degree in Applied and Computational Mathematics from the Universidade Federal do Rio Grande do Sul, Porto Alegre, Brazil before completing his PhD in modelling dynamic forces at the University of Melbourne. Since joining the Institute of High Performance Computing in Singapore in 2008 he continues his interest in modelling dynamic phenomena of deformable drops and bubbles and in improving his rating in correspondence chess and strike rate on the soccer pitch.

between interacting drops and bubbles that may precede possible coalescence and those experiments that measure the time dependent force acting between drops and bubbles in relative motion. We also review theoretical models to a sufficient level of detail to give a clear sense of the key underlying physical assumptions and indicate how such models take into account the initial and boundary conditions appropriate to each type of experiment.

The current state of theoretical modelling comprises mainly of numerical parametric studies without detailed reference to experimental data. Where comparisons are made, only data from a single experimental technique are used. We have therefore gathered experimental data obtained from researchers located in different continents and acquired in different centuries, using a variety of different but complementary methods to study drop–drop, bubble–bubble and drop or bubble-against-solid interactions. We hope that quantitative comparisons of theoretical predictions with a broad range of experimental results will provide a better appreciation of the underpinning physics of drainage and coalescence phenomena.

The review closes with a discussion of unsolved and unresolved problems in the area. Issues and directions in experimental methods and in theoretical model development where further work is needed are also identified.

1.3 Historical perspective

Experimental investigations of the time dependent interaction between a deformable bubble and a flat plate by Derjaguin and Kussakov[4] actually predated the formulation of the DLVO theory of colloidal stability by Derjaguin–Landau[5] and Verwey–Overbeek.[6] By observing the time evolution of the interference fringes formed by the water film between a bubble rising under buoyancy force towards a horizontal glass plate or mica sheet, Derjaguin and Kussakov were able to deduce that a non-equilibrium film profile forms a dimple.[4] Although experimental limitations did not allow them to make quantitative estimates of the film thickness, they did point out the significance of the barrier rim of the dimple in controlling the time taken for the rising bubbles to reach the equilibrium state against the plate.

The most basic model needed to capture the key physics of surface deformations and film drainage requires a description in terms of coupled partial differential equations.[7] Although numerical solutions of the governing equations have been demonstrated,[8–17] sometimes for somewhat artificial initial and boundary conditions, no substantial progress has been made in direct quantitative comparisons with experiments. Also, many of these theoretical model studies assume that the interface of the drops or bubbles cannot sustain any shear stress in what is sometimes referred to as the fully mobile interface. But as we shall see, the dynamic response of such interfaces in many experimental studies suggests that the interfaces of the drops or bubbles behave more often than not as tangentially immobile surfaces.

Paradoxically, the success of the DLVO theory in being able to explain the stability of suspensions of solid particles in terms of a balance of equilibrium surface forces led subsequent studies of film drainage and interactions involving bubbles and drops to perhaps overlook the importance of interfacial deformations and hydrodynamic effects.[18] In fact, transient phenomena were generally considered using the Reynolds Flat Film Model[19,20] that is attractive because a simple analytical solution is available.[21] The flat film assumption of this model also meant that only until recently, there were few experimental attempts to investigate and quantify the spatial and temporal variations of deforming and draining films. Moreover, the shortcomings of the original Reynolds Flat Film Model gave rise to a number of increasingly complex theoretical extensions[22–28] that were not capable of giving quantitative agreement with results of very detailed experiments.[2,29–52]

A number of empirical analytical results[53–56] has been developed to describe film drainage behaviour, unfortunately none gave quantitative agreement when compared to experiments.[30]

2. Experimental studies

'*Theory without experiment is useless.*' I. B. Ivanov.[57]

We first summarise different experimental approaches that have been used to study film drainage and time dependent interactions involving drops and bubbles. These techniques fall into three broad categories.

(1) Time variations in thickness of the film between drops and bubbles during interaction can be obtained by recording the optical interference fringe patterns produced by the deformed interfaces. Such fringe patterns can be processed to extract *variations of the local thickness with time and with position* along the film. When combined with information about how the drops or bubbles are being driven, this approach provides valuable data for comparison with theory.

(2) Direct measurements of the *time-dependent forces* between any pairing of drops, bubbles and solid particles as they are moved together or separated in a controlled fashion in the atomic force microscope. By driving the interacting bodies in different prescribed ways, variations of the coalescence time, if coalescence occurs, can also be determined.

(3) Drop–drop interactions can be characterised by the *coalescence time* when they are driven together under externally imposed flow fields. This provides somewhat less detailed information about the interaction dynamics than the previous two approaches as neither deformations nor film thicknesses can be measured with precision.

Although there have been many studies of drop/bubble interactions and the associated phenomenon of film drainage and coalescence, experimental data obtained under well-defined conditions and suitable for quantitative analysis have only become available in the past decade or so. This review will focus on the comparison between theory and examples of such experiments as summarised below.

2.1 Emerging drops/bubbles from capillaries

This technique focuses on the interaction between two bubbles or drops in a surrounding fluid. The bubbles or drops are formed at the ends of two opposing sealed capillary tubes that share a common axis. The emergent drops or bubbles are then moved towards each other by displacing the capillary tubes axially at a known rate.[31] Thinning and deformations of the film between the drops/bubbles are monitored by optical interference

methods. If the drops/bubbles are brought together by injecting fluid or air into the capillaries, the rate of inflation must be measured accurately to permit quantitative analysis.[58]

2.2 Bubble on solid

Due to the relevance to mineral flotation processes, bubble–solid interactions in water are of special interest. One way of studying the approach of a bubble to a surface is to allow it to rise under constant buoyancy force.[59–63] Optical interference techniques can be used to monitor the drainage of the water film trapped between the bubble and the surface. Another method is to force an emerging bubble from a capillary against a solid plate where the axis of the capillary is oriented normal to the plate.[2,29,30] Monitoring time variations of the intensity of reflected light at different positions provides spatial and temporal information about the water film between the bubble and the solid. Proper characterisation of how the bubble is driven towards the surface is required for quantitative analysis. This method operates at low capillary pressures in the range of 100 Pa.

2.3 Mercury drop on solid

A very accurate method that tracks the evolution of both the spatial and temporal variations of the thickness of a water film trapped between a flat mica surface and a liquid drop is to monitor the variations in fringes of equal chromatic order.[33,34,39] Using a mercury drop with high reflectivity, this method is capable of resolving film thicknesses with sub-nanometre precision. As mercury is also a conductor it is possible to adjust the electrostatic interaction between the mercury drop and the charged mica surface to explore both repulsive and attractive electrical double layer interactions between the solid and the mercury. Therefore this system can be used to study the behaviour of stable and unstable draining films. In addition, unexpected and novel spatial and temporal responses of a stable film to mechanical and electrical perturbations can also be quantified.[37]

2.4 Scheludko cell

The Sofia School has pioneered the study of film drainage by monitoring the film trapped between two opposing menisci formed inside a cylindrical cell—the Scheludko cell.[18] The interfaces are driven together by withdrawing the liquid in the cell between the menisci. Although this experimental system has been used to study liquid/liquid and gas/liquid systems as well as the effects of different chemical additives, quantitative details of the film profile and liquid withdrawal conditions are often not reported. As experimental results from the Scheludko cell are almost always interpreted in terms of the Stefan–Reynolds Flat Film Model (see Section 6)[19,20] the general focus is to consider only the "average" film thickness rather than the detailed spatial variations of the position of the film interface.

2.5 Atomic force microscope measurements

In contrast to all aforementioned experimental methods that are concerned with film geometry, the atomic force microscope has been used to measure time dependent forces between pairs of drops, bubbles, solid particles and flat surfaces in relative motion. A drop/bubble/particle is attached at one end of a micro-cantilever and the other end is moved by a piezo-electric motor at a preset displacement pattern relative to the other drop, bubble or surface.[64–66] Time variations of the force are obtained from recorded deflections of the cantilever. Although there is sufficient information available to model the force without adjustable parameters, information about drop or bubble deformations is not directly accessible.

A robust model of time dependent film drainage and interaction between drops and bubbles should be able to account for data from the various types of experiments mentioned above without fitting parameters.

3. Theoretical models

'*Experiment without theory is meaningless.*' I. B. Ivanov.[57]

Three essential elements are required to understand time-dependent interactions involving deformable drops and bubbles:

(a) a description of how drops/bubbles deform and give rise to characteristic geometric motifs such as the "pimple", "dimple" and "wimple",

(b) a description of the time and position dependent hydrodynamic interaction arising from film drainage, and

(c) the nature of surface or colloidal forces between interfaces in close proximity that will determine collision stability or coalescence.

There are many attempts in the literature to include these elements with varying degrees of sophistication and technical complexity. The exposition in this section will concentrate on the simplest fundamental aspects of each of these physical features and show how they can be assembled to form a coherent description. We will return to a more detailed discussion of different theoretical models in Section 6 after comparing the prediction of one such model with a range of experiments. Hereafter what we ascribe to drops will apply equally to bubbles. The ideas developed for two drops also apply to head-on collisions between a drop with a spherical particle or for normal collision between a drop and a flat solid surface.

A head-on collision event between two drops in a suspending medium can be separated into the following stages. Initially, the drops travel at some known velocity under an external force, F_{ext}, that drives the collision. When the separation between the centres of mass falls below the value at which the drops would touch if they had retained their original shapes, the surfaces of the drops around the region of closest approach must deform. If there is a repulsive force between the surfaces of the drops, their interfaces will flatten. A thin film of the suspending medium will be trapped between the drops and we can then speak of the commencement of the film drainage stage. The drainage dynamics, such as whether the film will develop a pimple or a dimple or whether the drainage process will lead to coalescence, is determined by a number of factors. These include the initial separation, the manner by which the drops are driven together, the physical parameters of the system such as viscosity and surface tension, the nature of hydrodynamic flow in the thin film and the form of any surface forces (*e.g.* Van der Waals, electric double layer) that operate between the drops.

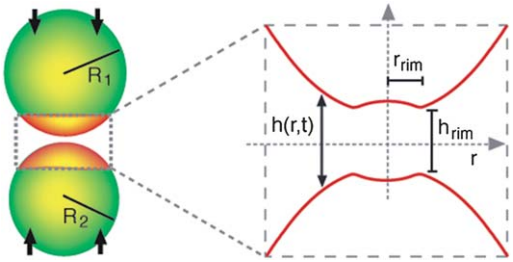

Fig. 1 Schematic illustration of the axisymmetric inner region of the interaction zone with a dimple between approaching drops comprising of the film of variable thickness h and radius r_{rim} that are both small compared to the drop dimensions: R_1, $R_2 \gg r_{rim} \gg h$.

For example, the Van der Waals interaction between two identical drops in a continuous phase is attractive. If other surface forces such as electrical double layer or steric repulsion cannot provide a sufficiently repulsive barrier, the film will drain and rupture and the two drops will coalesce. At very low approach speeds a pimple will form before coalescence, whereas at higher approach speeds, the formation of a hydrodynamic dimple (Fig. 1) will precede coalescence. However, if the initial kinetic energy of the drops is sufficiently high for inertial effects to be important, the drops may rebound after the collision.

If the surface forces between the drops are sufficiently repulsive, the equilibrium configuration under a constant external force, F_{ext}, will be one in which the two drops are separated by a nearly parallel flat film of thickness h_{eq} and radius a. The equilibrium force balance condition can be expressed as:

$$F_{ext} = \pi a^2 \Pi(h_{eq}) \quad (1)$$

where $\Pi(h)$ is the repulsive disjoining pressure that gives rise to a stable film. For a given external force, F_{ext}, and the functional form of the disjoining pressure, $\Pi(h)$, the as yet unknown film radius, a, and equilibrium film thickness, h_{eq}, can be determined by specifying how the drop deforms due to externally applied forces. In Section 3.1.5 we will see how the interaction zone or film radius, a, emerges naturally when we examine drop deformation under the Young–Laplace model.

By observing bubbles of radius, R_o (~1 mm), and interfacial tension, σ, being pushed against a horizontal flat plate by buoyancy force, Derjaguin and Kussakov[4] equated the external force, F_{ext}, to the buoyancy force and the unknown equilibrium disjoining pressure, $\Pi(h_{eq})$, to the Laplace pressure $(2\sigma/R_o)$ of the drop and verified the applicability of eqn (1) for the relation between the bubble radius, R_o, and the measured film radius, a.

More generally, there are three quite different characteristic length scales relevant to dynamic interactions involving deformable drops: millimetre for the drop radii, R, micrometre for the dimpled film radius, r_{rim}, and nanometre for the film thickness, h (Fig. 1). Thus the need to describe phenomena accurately over six orders of magnitude in length scale presents very significant challenges when direct numerical computations are used to model such interactions.

However, the detailed physics that determine interactions involving deformable drops occur in the neighbourhood of the thin film (Fig. 1). Provided the drop radius is much larger than the film radius, *i.e.* $R \gg r_{rim}$, we can develop a model that will allow us to focus only on the detailed drainage phenomenon within the film, while effects on the scale of the drop radius can be accounted for in terms of boundary conditions on the equations that govern film drainage. Such boundary conditions are also determined in part by the way the drops are driven together. In the remainder of this section we will develop such a model.

This review will mainly be concerned with film drainage phenomena at low Reynolds numbers where inertial effects are not important in hydrodynamic interactions. The fact that the drop radius, film radius and film thickness have very different characteristic dimensions allows the use of the lubrication approximation to describe hydrodynamic phenomena in the film.

We assume drop deformations during interaction are determined by the balance between the combination of hydrodynamic pressure due to flow in the film and disjoining pressure due to surface forces that tend to distort the drop shape, and capillary forces that minimise the interfacial area. Implicit in this model is that the response time of the drop due to capillary action is much faster than characteristic times in the variation of the hydrodynamic pressure and film thickness. If the interfacial tension of the drops is constant, this is a reasonable assumption. However, if the interface contains mobile surface-active species with characteristic diffusion times along the surface and possible molecular transport times to and from the interface, the characteristic time scales of such phenomena must also be considered.

As a base model, we assume constant interfacial tensions and see how well this accounts for a broad variety of experiments. The few parameters needed to specify such a model can be determined by independent measurements so that there are no free variables available to fit experimental data. As most of the experiments have been designed to study head-on interactions, we may also assume axial symmetry. This base model has two complementary parts: one to describe how a drop deforms as it is subjected to external forces that are localised within a small area on its surface and the other to describe fluid flows in the thin film between the drops where the thickness of the film is determined by the extent of drop deformation. Surface forces between the drops are taken from known equilibrium models.

3.1 Augmented Young–Laplace equation

The equilibrium deformation of a drop due the proximity of another drop or solid particle can be obtained by minimising the Helmholtz surface energy of the system. Consider a pendant drop on a substrate, immersed in a continuous medium as shown in Fig. 2. Surface force interactions between the drop and a flat surface (or another drop or a particle) at a distance D from the substrate are given in terms of an interaction free energy per unit area $E(h)$ or the corresponding disjoining pressure $\Pi(h) \equiv -\mathrm{d}E(h)/\mathrm{d}h$ that are known functions of the film thickness $h(r,t)$ around the axisymmetric drop. The Helmholtz surface energy, A_s, can be written in terms of the drop height $z(r,t)$:[67,68]

$$A_s = 2\pi \int_0^{r_1} \left[\sigma\sqrt{1+z_r^2} + \sigma_L - \sigma_S + E(h) - \Lambda z\right] r\,\mathrm{d}r \quad (2)$$

where $z_r \equiv \partial z/\partial r$. The first three terms in the integrand in eqn (2) represent the energies associated with the deformable surface of

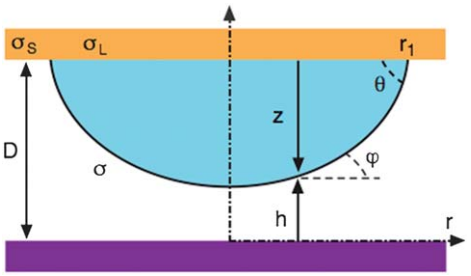

Fig. 2 Schematic of an axisymmetric pendant drop of constant surface tension, σ, on a substrate in which the interaction with a flat surface is concentrated within a small interaction zone around the apex.

the drop with interfacial tension or surface energy per unit area σ, the drop–substrate interface with surface energy per unit area σ_L and the medium–substrate interface per unit area with surface energy σ_S. The interaction free energy per unit area, $E(h)$, between the drop interface and the flat surface has a range of nanometres and therefore is expected to only affect the apex region of the drop. The final term $\Lambda z(r,t)$ in the integrand accounts for the constraint of constant drop volume on the energy minimisation, where the constant Λ is the Lagrange multiplier. As we expect to be concerned with drop sizes of a millimetre or smaller, we have omitted the gravitational contribution to the free energy.

We work with the film thickness $h(r,t) = D(t) - z(r,t)$ and consider the perturbation $h(r,t) \rightarrow h(r,t) + \delta h(r,t)$ in eqn (2) using the calculus of variations. By requiring the first order variation δA_s to vanish we obtain the augmented Young–Laplace equation for the equilibrium film shape ($h_r \equiv \partial h/\partial r$):

$$\sigma(\kappa_1 + \kappa_2) \equiv \frac{\sigma}{r}\frac{\partial}{\partial r}\left(\frac{rh_r}{(1+h_r^2)^{1/2}}\right) = \frac{2\sigma}{R_L} - \Pi(h) \qquad (3)$$

We make the replacement $\Lambda \equiv (2\sigma/R_L)$, where the constant R_L so-defined is the Laplace radius. The Lagrange multiplier, Λ, is the capillary pressure or the pressure difference between the interior and the exterior of the drop. In the absence of interactions, the disjoining pressure vanishes, $\Pi(h) \rightarrow 0$, and the pendant drop shape will be a portion of a sphere of radius R_o and the constant $R_L \rightarrow R_o$. This gives the expected expression for the capillary pressure ($2\sigma/R_o$) of an unperturbed drop. The magnitude of the constant R_L is therefore of the order of the unperturbed drop radius.

The derivative in eqn (3) is the sum of the two principal curvatures: κ_1 in the plane of Fig. 2 and κ_2 the circumferential curvature of the axisymmetric drop surface. A repulsive interaction that corresponds to $\Pi(h) > 0$ will flatten or reduce the curvature of the drop at the apex, so interactions under constant volume will change the capillary pressure as reflected in deviations of R_L from R_o.

Variations in the end point, $r_1 \rightarrow r_1 + \delta r_1$ (see Fig. 2), of the surface energy of the attached pendant drop given by eqn (2) yields the Young–Dupre condition: $\sigma \cos\theta + \sigma_L = \sigma_S$ for the equilibrium contact angle θ, since $\Pi(h) = 0$, at the base of the drop which is far from the interaction zone.

The derivation of the augmented Young–Laplace equation (eqn (3)) *via* energy minimisation assumes the drop is at equilibrium. In the presence of hydrodynamic interactions, we make the reasonable assumption that the drop can adjust its shape instantaneously to accommodate changes in the hydrodynamic and disjoining pressure. This is plausible as long as changes in velocities of these perturbations are much slower than the speed of propagation of interfacial disturbances around the drop.§ Thus we can add the effects of the hydrodynamic pressure, p to the rhs of eqn (3) to give

$$\frac{\sigma}{r}\frac{\partial}{\partial r}\left(\frac{rh_r}{(1+h_r^2)^{1/2}}\right) \equiv \frac{\sigma}{r}\frac{\partial}{\partial r}(r\sin\varphi) = \frac{2\sigma}{R_L} - \Pi(h(r,t)) - p(r,t) \qquad (4)$$

If the hydrodynamic pressure is repulsive ($p > 0$), it will flatten the interacting zone around the drop apex. We have also expressed the curvature in terms of the tangent angle, φ, where $h_r \equiv \partial h/\partial r \equiv \tan\varphi$, see Fig. 2. Eqn (4) can also be derived by a balance of normal forces against surface tension forces on a surface element by a quasi-static treatment of the hydrodynamic pressure.

In the remainder of this section, we shall develop the solution of the Young–Laplace equation (eqn (4)) in terms of an inner solution that describes details of drop deformations resulting from the disjoining pressure and hydrodynamic pressure on the nanometre to micrometre scale. We also demonstrate how this inner solution is coupled *via* drop volume conservation to the outer solution that describes deformations on the scale of the drop radius. Without the ability to split the problem into an inner and outer solution, a direct numerical solution of eqn (4) would require an algorithm that can cope with deformations that vary over six orders of magnitude in length scale.

3.1.1 Drop shape outside the interaction zone. A number of important general results concerning drop deformation can be deduced by taking the first integral of eqn (4) with respect to r to give

$$r\sin\varphi = \frac{r^2}{R_L} - \frac{1}{2\pi\sigma}\Phi(r,t) \qquad (5)$$

$$\Phi(r,t) \equiv 2\pi\int_0^r [p(r',t) + \Pi(r',t)]r'\mathrm{d}r' \qquad (6)$$

The function $\Phi(r,t)$ is related to the total force, $F(t)$:

$$F(t) = 2\pi\int_0^\infty [p(r',t) + \Pi(r',t)]r'\mathrm{d}r' \equiv \Phi(\infty,t) \qquad (7)$$

that acts on the drop due to the hydrodynamic and the disjoining pressures, p and Π respectively. At positions outside the interaction zone that corresponds to $r \gg r_{rim}$, both p and Π are negligibly small, and eqn (5) for the drop shape becomes (Fig. 1)

§ Capillary waves of velocity c and wavelength λ on a spherical drop obey the dispersion relation: $c^2 = 2\pi\sigma/[\lambda(\rho_d + \rho_e)]$, where σ is the interfacial tension, ρ_d and ρ_e the densities of the dispersed and continuous phases.[135] Taking $\lambda \approx 100$ μm, the dimension of the deformation zone gives $c \approx 1$ m s^{-1}, which is much greater than characteristic approach velocities of drops considered here.

$$r\sin\ \varphi = \frac{r^2}{R_L} - \frac{F(t)}{2\pi\sigma}, \quad \text{for } r \gg r_{\text{rim}} \tag{8}$$

This result does not depend on the detailed forms of p and Π in the interaction zone. Thus provided the extent of interaction zone is small on the scale of the drop radius, the drop shape outside the interaction zone only depends on the total force $F(t)$ as it appears in eqn (8). This is a key observation that provides the necessary boundary condition that governs film deformation during interaction (see Section 3.2).

3.1.2 Origin of the 'dimple', 'pimple', 'wimple' and 'ripple'. Eqn (5) and (6) also give a physical demonstration between forces acting on the drop and the geometric characteristics of resulting deformations.

Since $\Phi(0,t) = 0$, the drop always has zero slope at the apex $r = 0$ as expected from the assumption of axial symmetry. In the absence of interactions, which corresponds to $\Phi(r,t) = 0$, we have, from eqn (5), $\sin\varphi > 0$ for $r > 0$, so the shape of the drop will always be concave up as illustrated in Fig. 2.

In general, the magnitude of $\Phi(r,t)$ is bounded and approaches the constant value $F(t)$ for $r \gg r_{\text{rim}}$, see eqn (7). Therefore, the curvature of the drop shape in Fig. 2 must be concave up outside the interaction zone. However, within the interaction zone, the term $[(2\pi\sigma r^2/R_{\text{L}}) - \Phi(r,t)]$ determines the possible formation of deformations such as the 'pimple', 'dimple' or 'wimple'.

(1) *Pimple*: if $[(2\pi\sigma r^2/R_{\text{L}}) - \Phi(r,t)] > 0$ for all r, the drop shape will have a 'pimple'[69] (Fig. 3) provided its derivative with respect to r has two zeroes at $0 < r_1^* < r_2^*$ in addition to a zero at $r = 0$, a condition that is equivalent to having two solutions of $2\sigma/R_{\text{L}} = (p + \Pi)$ at r_1^* and r_2^* where the total pressure is equal to the Laplace pressure.

(2) *Dimple*: if $[(2\pi\sigma r^2/R_{\text{L}}) - \Phi(r,t)]$ has a zero at $r^* > 0$, but is negative for $0 < r < r^*$, and positive for $r > r^*$, the drop shape will have a 'dimple'[70] (Fig. 3).

(3) *Wimple*: if $[(2\pi\sigma r^2/R_{\text{L}}) - \Phi(r,t)]$ has two zeroes at r_1^* and r_2^*, but is negative for $r_1^* < r < r_2^*$, then the drop shape will exhibit a 'wimple'[37] (Fig. 3).

(4) *Ripple*: the interface can exhibit additional pairs of maxima and minima[71] as determined by the number of zeroes in the function $[(2\pi\sigma r^2/R_{\text{L}}) - \Phi(r,t)]$. In physical terms, this is controlled by the spatial variation of the integral of the sum of the hydrodynamic pressure, p, and the disjoining pressure, Π, as they appear in eqn (6).

The formation of the pimple, dimple or wimple follows directly from the spatial variation of the hydrodynamic and disjoining pressures that appear in the augmented Young–Laplace equation (eqn (5) and (6)). The hydrodynamic boundary condition at the drop surface only enters indirectly in determining the hydrodynamic pressure. This also explains why dimple formation has been observed in models with very different physical descriptions of the film drainage process.[31,72–77]

In qualitative terms, we can deduce from eqn (5) and (6) conditions under which a film can develop a pimple or dimple. For a pimple to develop, we must have $\Phi(r,t) < 0$. This can arise, for example, when the disjoining pressure Π is attractive (<0) and the hydrodynamic pressure p is small in magnitude (corresponding to slow moving drops) or when the hydrodynamic pressure p is large and negative (corresponding to fast separating drops) and the disjoining pressure Π is small. Of course, other combinations of magnitudes of p and Π that ensure $\Phi(r,t) < 0$ can also give rise to a pimple. Similarly, when $\Phi(r,t) > 0$, the drop will be flattened from the undeformed shape. However, when $[(2\pi\sigma r^2/R_{\text{L}}) - \Phi(r,t)] < 0$, there will be an inversion in the curvature and a dimple will develop. This can happen, for example, when Π is small and p is large and positive (for fast approaching drops). In fact, since in theory the hydrodynamic pressure can increase without bounds for approaching drops, a dimple will always form in the absence of a disjoining pressure although the separation when this happens can be unrealistically small if the approach velocity is very low. We will see experimental examples of such film deformations in Section 4.

3.1.3 Inner equation and asymptotic solution. We now summarise the different forms of the augmented Young–Laplace equation for the film thickness, h, between: (i) a drop (or bubble) and a flat wall, (ii) a drop and a spherical solid particle and (iii) between 2 drops.

(i) Drop/bubble against flat wall. Within the interaction zone or the inner region defined by the interval $r = 0$ to $r \approx r_{\text{rim}}$, the drop interface is relatively flat on the scale of the drop size. So to a good approximation: $\sin\varphi \approx \partial h/\partial r \ll 1$, so the augmented Young–Laplace equation (eqn (4)) can be linearised to give

$$\frac{\sigma}{r}\frac{\partial}{\partial r}\left(r\frac{\partial h}{\partial r}\right) = \frac{2\sigma}{R_L} - \Pi - p \quad \text{(drop–wall)}. \tag{9}$$

Given the disjoining pressure, Π, and the hydrodynamic pressure, p, the thickness of the inner region of the film, h, as a function of position r can be found by integrating this equation—in general, numerically.

However, by formally integrating eqn (9) with respect to r twice from 0 to r we obtain the result

$$h(r,t) = h(0,t) + \frac{r^2}{2R_L} - \frac{1}{2\pi\sigma}\log\left(\frac{r}{2R_o}\right)\Phi(r,t) + \frac{1}{2\pi\sigma}\Xi(r,t) \tag{10}$$

$$\Xi(r,t) \equiv 2\pi\int_0^r [p(r',t) + \Pi(r',t)]r'\log\left(\frac{r'}{2R_{\text{o}}}\right)\mathrm{d}r' \tag{11}$$

where $h(0,t)$, the film thickness at $r = 0$, has yet to be determined. The characteristic length scale in this drop-flat wall problem is the Laplace radius, R_{L} in eqn (9). However, in the logarithmic term in eqn (10) and (11) we have chosen the known radius of the undeformed drop, R_{o}, as the scaling factor as we shall be using

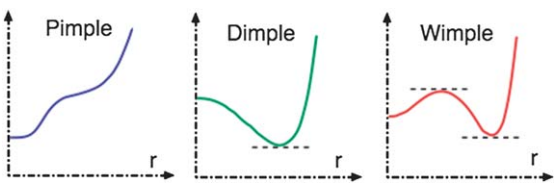

Fig. 3 Commonly observed shapes, pimple, dimple and wimple, of the interface of deformable drops and bubbles.

these results in the regime when the extent of the deformation is small compared to the size of the drop and so we have $R_L \approx R_o$.

We observe that for $r > r_{rim}$, the film thickness, h, will become large so the corresponding magnitudes of Π and p will be small. Therefore for $r > r_{rim}$, we can replace the upper limits in the integrals in eqn (6) and (11) by infinity to obtain the outer asymptotic form of $h(r,t)$ in terms of the force, $F(t)$, defined by eqn (7), acting on the drop

$$h(r,t) \to h(0,t) + \frac{r^2}{2R_L} - \frac{F(t)}{2\pi\sigma}\log\left(\frac{r}{2R_o}\right) + H(R_o,t), \quad r > r_{rim} \tag{12}$$

$$H(R,t) \equiv \frac{1}{\sigma}\int_0^\infty \left[p(r',t) + \Pi(r',t)\right] r' \log\left(\frac{r'}{2R}\right) dr' \tag{13}$$

In Section 3.1.4, we will see that the logarithmic behaviour for $r > r_{rim}$ in eqn (12) will match up with the inner asymptotic behaviour of the outer solution of the augmented Young–Laplace equation (eqn (8)). What is significant here is that the total force, $F(t)$, acting on the drop is encoded in the geometric shape or deformation of the film outside the interaction zone. This logarithmic limiting form of the film thickness has been observed experimentally.[78] This result is analogous to Hooke's Law for a linear spring where the force exerted on the spring can be deduced from the extension.

(ii) Drop/bubble against a spherical particle. For a drop or bubble interacting with a solid sphere of radius R_s, the film thickness, h, has to account for variations in the shape of the sphere (see Fig. 4) and so the drop height, z, is given by: $z(r,t) = D(t) + r^2/(2R_s) - h(r,t)$. By the same calculus of variation calculation that led to eqn (3) followed by linearisation in the inner region where $\partial h/\partial r \ll 1$, we obtain the inner form of the (linearised) augmented Young–Laplace equation:

$$\frac{\sigma}{r}\frac{\partial}{\partial r}\left(r\frac{\partial h}{\partial r}\right) = \frac{2\sigma}{R_{ds}} - \Pi - p \quad \text{(drop–sphere)} \tag{14}$$

where $R_{ds} \equiv (1/R_L + 1/R_s)^{-1}$. In the same manner as we derived eqn (10), (11) and (12), we find for $r > r_{rim}$

$$h(r,t) \to h(0,t) + \frac{r^2}{2R_L} - \frac{F(t)}{2\pi\sigma}\log\left(\frac{r}{2R_{dso}}\right) + H(R_{ds},t), \quad r > r_{rim} \tag{15}$$

with $R_{dso} \equiv (1/R_o + 1/R_s)^{-1}$.

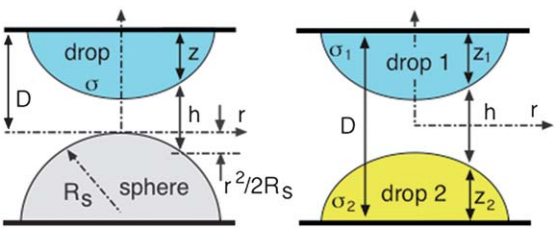

Fig. 4 Definition of the film thickness h between a drop/bubble and a spherical particle or between two drops/bubbles.

(iii) Two drops or bubbles. For the interaction between two drops (or bubbles) whose shapes are given by $z_1(r,t)$ and $z_2(r,t)$ (see Fig. 4) we have to minimise the surface energies of both drops with interfacial tensions σ_1 and σ_2, and capillary pressures $(2\sigma_1/R_{L1})$ and $(2\sigma_2/R_{L2})$. The resulting augmented Young–Laplace equations, after linearisation in the inner region where $\partial z_1/\partial r$, $\partial z_2/\partial r \ll 1$, can be combined in terms of the film thickness, h, using the geometric relation: $z_1 + z_2 = D - h$ (see Fig. 4) to give[7]

$$\frac{1}{2}\frac{\bar\sigma}{r}\frac{\partial}{\partial r}\left(r\frac{\partial h}{\partial r}\right) = \frac{2\bar\sigma}{\bar R} - \Pi - p \quad \text{(drop–drop)} \tag{16}$$

The constants $\bar R$ and $\bar\sigma$ are defined by

$$\frac{1}{\bar R} \equiv \frac{1}{2}\left(\frac{1}{R_{L1}} + \frac{1}{R_{L2}}\right) \quad \text{and} \quad \frac{1}{\bar\sigma} \equiv \frac{1}{2}\left(\frac{1}{\sigma_1} + \frac{1}{\sigma_2}\right)$$

Note the additional factor (1/2) on the lhs of eqn (16) for this two drops case. The outer asymptotic form for $r > r_{rim}$ is given by

$$h(r,t) \to h(0,t) + \frac{r^2}{\bar R} - 2\left(\frac{F(t)}{2\pi\bar\sigma}\right)\log\left(\frac{r}{2\bar R_o}\right) + 2H(\bar R_o,t), \quad r > r_{rim} \tag{17}$$

with the scale factor $\bar R_o \equiv 2/(1/R_{1o} + 1/R_{2o})$, chosen as before in terms of the unperturbed radii of the two drops. Eqn (17) has the same logarithmic form as eqn (12) and (15) with the force $F(t)$ as the pre-factor except for an additional factor of 2.

3.1.4 Outer asymptotic solution. The unknown quantities $h(0,t)$ and $H(R,t)$ that appear in the outer asymptotic form of the inner solution $h(r,t)$ given by eqn (12), (15) and (17) can be found by first solving eqn (8) for the drop shape outside the interaction zone and then matching this to the inner solution.

In Appendix A, we derive an analytic solution of the outer solution valid to linear order in the parameter $F/(2\pi\sigma R_L) \ll 1$ which is applicable when the extent of drop deformations arising from interactions is small on the scale of the drop size—a condition that is well satisfied for all the experiments we examine in Sections 4 and 5. From eqn (A14) and (A16), the limiting form of the shape of the drop as one approaches the interaction zone from the *outside* is

$$\begin{aligned} z(r,t) \to{}& R_o(1-\cos\ \theta_o) - \frac{r^2}{2R_L} \\ &+ \frac{F(t)}{2\pi\sigma}\left\{\log\left(\frac{r}{2R_o}\right) + B(\theta_o)\right\}, \quad r \to r_{rim} \end{aligned} \tag{18}$$

$$B(\theta) = \begin{cases} 1 + \dfrac{1}{2}\log\left(\dfrac{1+\cos\ \theta}{1-\cos\ \theta}\right) & \text{pinned } r_1 \\ 1 + \dfrac{1}{2}\log\left(\dfrac{1+\cos\ \theta}{1-\cos\ \theta}\right) - \left(\dfrac{1}{2+\cos\ \theta}\right) & \text{constant } \theta_o \end{cases} \tag{19}$$

This result depends on whether the drop deforms with a pinned three phase contact line at position r_1 (see Fig. 2) or with a constant contact angle θ_o. The general case in which both the contact line and the contact angle change is expected to lie between these two limits.

We now match these results to the inner solution in eqn (12) and (17) at $r \approx r_{rim}$ in order to determine the unknown constants $h(0,t)$ and $H(R,t)$, and the film thickness $h(r,t)$ just beyond the film radius $r \geq r_{rim}$.

(i) Drop/bubble against flat wall. For the interaction between a drop and a solid flat surface, we have $h(r,t) = D(t) - z(r,t)$ (see Fig. 2), so the unknowns $h(0,t)$ and $H(t)$ in eqn (12) for the asymptotic form of $h(r,t)$ valid for $r \geq r_{rim}$ can be eliminated using eqn (18) to give

$$h(r,t) \cong D(t) - R_o(1-\cos\ \theta_o) + \frac{r^2}{2R_L} - \left(\frac{F(t)}{2\pi\sigma}\right)\left\{\log\left(\frac{r}{2R_o}\right) + B(\theta_o)\right\}, \quad r \geq r_{rim} \tag{20}$$

The unknown constants of the inner solution in eqn (12) $h(0,t) + H(R_o,t) = D(t) - R_o(1 - \cos\ \theta_o) - F(t)B(\theta_o)/(2\pi\sigma)$, follow from eqn (12) and (20). This completes the demonstration of the matching between the inner and the outer solution. Likewise we can match the corresponding results for interaction configurations of a drop/bubble against a spherical particle and between two drops or bubbles.

(ii) Drop/bubble against a spherical particle. For a drop or bubble interacting with a solid sphere, we have the geometric relation $h(r,t) = D(t) + r^2/(2R_s) - z(r,t)$ where R_s is the sphere radius and $D(t)$ is the position of the apex of the solid sphere (Fig. 4). Thus the form of $h(r,t)$ valid for $r \geq r_{rim}$ is with $R_{ds} \equiv (1/R_L + 1/R_s)^{-1}$,

$$h(r,t) \cong D(t) - R_o(1-\cos\ \theta_o) + \frac{r^2}{2R_{ds}} - \left(\frac{F(t)}{2\pi\sigma}\right)\left\{\log\left(\frac{r}{2R_o}\right) + B(\theta_o)\right\}, \quad r \geq r_{rim} \tag{21}$$

(iii) Two drops or bubbles. The geometric relation between the heights, z_1 and z_2, of two interacting drops and the separation, D, between the substrates is $h(r,t) = D(t) - z_1(r,t) - z_2(r,t)$ (Fig. 4) so the asymptotic form of $h(r,t)$ for $r \geq r_{rim}$ is

$$h(r,t) \cong D(t) - R_{1o}(1-\cos\ \theta_{1o}) - R_{2o}(1-\cos\ \theta_{2o}) + \frac{r^2}{\bar{R}} - \left(\frac{F(t)}{2\pi\sigma_1}\right)\left\{\log\left(\frac{r}{2R_{1o}}\right) + B(\theta_{1o})\right\} - \left(\frac{F(t)}{2\pi\sigma_2}\right)\left\{\log\left(\frac{r}{2R_{2o}}\right) + B(\theta_{2o})\right\}, \quad r \geq r_{rim} \tag{22}$$

As we shall see, the results in eqn (20)–(22) provide the vital link between the way the drop is moved as specified by the separation $D(t)$ and the value for $\partial h/\partial t$ at some position r_{max} ($>r_{rim}$) outside the interaction zone. Therefore the manner in which the drops are driven as characterised by the function $D(t)$ will appear as a boundary condition for the inner equation that governs the evolution of drop deformations in the interaction zone.

In addition, if the interaction is repulsive, that is $F(t) > 0$, so that the drops will flatten around the interaction zone, it is possible to derive general analytic force–displacement formulae from eqn (20)–(22) that describe how drops deform under a constant volume constraint.

3.1.5 Force–displacement relation for deforming drops. From the inner form of the augmented Young–Laplace equations that describe the film thickness, h, for various geometries given by eqn (9), (14) and (16) we can identify the position at which $\partial h/\partial r = 0$ as the film radius a at each interaction geometry. And by evaluating eqn (20)–(22) at $r = a$, we can obtain the corresponding force–displacement relations.

(i) Drop/bubble against flat wall. By integrating the inner form of the augmented Young–Laplace equation (eqn (9)) for a drop against a flat wall with respect to r, we have $\partial h/\partial r = 0$ at $r = a \equiv [F(t)R_L/2\pi\sigma]^{1/2}$. We evaluate eqn (20) at the interaction zone radius a to find

$$\Delta D(t) \equiv D(t) - R_o(1-\cos\ \theta_o) - h(a,t) \cong \frac{F(t)}{4\pi\sigma}\left\{\log\left(\frac{F(t)R_L}{8\pi\sigma R_o^2}\right) + 2B(\theta_o) - 1\right\} \tag{23}$$

By approximating the Laplace radius $R_L \approx R_o$ in the logarithm term, this gives a very useful approximate relation between the force, F, and the relative displacement, ΔD (see Fig. 2) that reflects the deformation of the drop under a constant volume constraint that has been imposed in the derivation of eqn (18) in Appendix A. In practice, the film thickness $h(a,t)$ is small compared to the other quantities and so eqn (23) relates the force, F, to the relative displacement ΔD which is a control variable in a force measurement experiment. Eqn (23) is very useful for checking experimental force measurements that involve deformable drops and bubbles as all the physical parameters such as the interfacial tension, σ, drop radius, R_o, and contact angle, θ_o, can be measured independently.

We note that the non-linear force–displacement relation (eqn (23)) follows from the solution of the Young–Laplace equation and implies that a drop or bubble does not behave as a Hookean spring under deformation as often assumed.[64,65,79] Furthermore this result is independent of the details of the repulsive disjoining pressure which determines the magnitude of the film thickness $h(a,t)$, that is small in comparison to the separation D in eqn (23). In other words, for repulsive interactions, measuring the static or equilibrium force–displacement relationship will provide information about the interfacial tension σ, the drop radius R_o and the contact angle θ_o. However, the result will be insensitive to the detailed form of the repulsive disjoining pressure.

The force–displacement relation, eqn (23), will hold for repulsive interactions provided the deformation is a small fraction of the drop radius.

In a similar manner, we can derive similar approximate analytic force–displacement formula for the repulsive interaction between a drop/bubble and a spherical particle or between two drops/bubbles. These results are given below.

(ii) Drop/bubble against a spherical particle. By integrating the inner form of the augmented Young–Laplace equation (eqn (14)) for a drop against a spherical particle of radius, R_s, we have $\partial h/\partial r = 0$ at $r = [F(t)R_{ds}/2\pi\sigma]^{1/2}$, where $R_{ds} \equiv (1/R_L + 1/R_s)^{-1}$.

The desired force–displacement formula follows from evaluating eqn (21) at $r = a \equiv [F(t)R_{ds}/2\pi\sigma]^{1/2}$,

$$\Delta D(t) \equiv D(t) - R_o(1 - \cos\ \theta_o) - h(a,t) \cong \frac{F(t)}{4\pi\sigma}\left\{\log\left(\frac{F(t)R_{ds}}{8\pi\sigma R_o^2}\right) + 2B(\theta_o) - 1\right\} \quad (24)$$

where we may approximate $R_{ds} \approx (1/R_o + 1/R_s)^{-1}$ in terms of the known unperturbed drop radius, R_o, and particle radius, R_s.

(iii) Two drops or bubbles. From the inner form of the augmented Young–Laplace equation in eqn (16) for two interacting drops, the film radius is at $r = a \equiv [F(t)\ \bar{R}/2\pi\bar{\sigma}]^{1/2}$. Evaluating eqn (22) at this position gives

$$\Delta D(t) \equiv D(t) - R_{1o}(1 - \cos\ \theta_{1o}) - R_{2o}(1 - \cos\ \theta_{2o}) - h(a,t) \cong \frac{F(t)}{4\pi\sigma_1}\left\{\log\left(\frac{F(t)\bar{R}}{8\pi\bar{\sigma}R_{1o}^2}\right) + 2B(\theta_{1o})\right\} + \frac{F(t)}{4\pi\sigma_2}\left\{\log\left(\frac{F(t)\bar{R}}{8\pi\bar{\sigma}R_{2o}^2}\right) + 2B(\theta_{2o})\right\} - \frac{F(t)}{2\pi\bar{\sigma}} \quad (25)$$

where we may approximate $\bar{R} \approx 2/(1/R_{1o} + 1/R_{2o})$ in terms of the known unperturbed drop radii, R_{1o} and R_{2o}.

(iv) Measurements on the atomic force microscope. To apply the above force–displacement formulae between a drop and a spherical particle (eqn 24) or between two drops (eqn 25) to force measurement experiments on the atomic force microscope (AFM), we have to relate the separation $D(t)$ to the position of the end of the cantilever $X(t)$ and the cantilever deflection $S(t)$ using the geometric condition (Fig. 5):

$$D(t) = X(t) + S(t) = X(t) + F(t)/K \quad (26)$$

where K is the spring constant of the cantilever.

Recall that the constant compliance response in AFM force measurements is used to estimate the absolute separation between interacting bodies that can come into "hard contact". For soft deforming bodies where the concept of "hard contact" does not exist, the combined results of eqn (26) and (24) or (25) provide the important replacement relation between the cantilever displacement and a repulsive interaction that also takes into account drop/bubble deformations. This repulsive interaction may be due to repulsive disjoining pressure at low approach speeds or may be dominated by repulsive hydrodynamic interactions at high approach speeds. The results in eqn (23)–(25) apply irrespective of how the repulsive force F has been generated.

We have extracted key physical information and behaviour about drop deformation according to the augmented Young–Laplace equation. From eqn (5) and (6) we demonstrated how various observed characteristic deformation shapes such as the pimple, dimple, wimple and ripple arise from the combined variations of the hydrodynamic and disjoining pressures. In practice, deformations arising from interactions are small compared to the drop dimensions, hence, the asymptotic analysis of the inner and outer region that resulted in eqn (20)–(22) enabled us to treat the outer solution as a boundary condition for the inner problem that has to be solved numerically. This circumvents the need to obtain numerical solutions that must resolve dimensions on the millimetre scale for drop sizes to the nanometre scale for film thicknesses. Deformations of the rest of the drop arising from the volume conservation constraint of the drop/bubble can be included as boundary conditions for the inner problem. Information about how the interacting drops are driven by external forces is contained in the function $D(t)$.

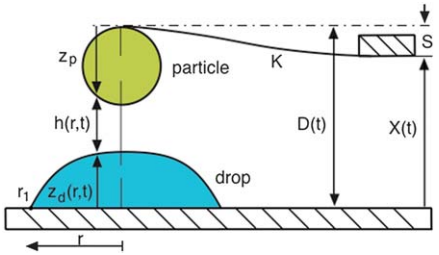

Fig. 5 The geometry of the atomic force microscope (AFM).

To completely determine the spatial and temporal evolution of drop deformations arising from interactions, we need to specify the hydrodynamic pressure $p(r,t)$ in order to solve eqn (9), (14) or (16). This will be discussed in the next section.

3.2 Stokes–Reynolds hydrodynamics

In experiments on drop–drop interactions and film drainage considered in this review, Stokes flow appropriate at low Reynolds number provides an adequate description. Since the film thickness is small compared to the radial extent of the film, the Reynolds lubrication theory[80,81] can be applied to describe hydrodynamic drainage in the deformable film. Within the axisymmetric film, the radial r-direction component of the velocity, u is dominant and the pressure, p, only varies in the radial r-direction. Under such conditions, flow within the film is described by the radial component of the Stokes equations:

$$\mu\frac{\partial^2 u(r,z,t)}{\partial z^2} = \frac{\partial p(r,t)}{\partial r} \quad (27)$$

where μ is the shear viscosity of the continuous medium.

The equation for the time evolution of the film thickness follows from integrating the continuity equation from $z = 0$ to $h(r,t)$ together with the kinematic condition on the film surface:

$$\frac{\partial h(r,t)}{\partial t} = -\frac{1}{r}\frac{\partial}{\partial r}\left(r\int_0^{h(r,t)} u(r,z,t)\mathrm{d}z\right) \quad (28)$$

If hydrodynamic boundary conditions are specified on the boundary of the film at $z = 0$ and $z = h(r,t)$, eqn (27) may be integrated with respect to z to find $u(r,z,t)$ in terms of $p(r,t)$. Substitution of the solution into eqn (28) will give an equation relating $h(r,t)$ and $p(r,t)$. This result, together with the appropriate augmented Young–Laplace equation given by eqn (9), (14) or (16), will provide a complete description of the spatial and temporal evolution of the film.

Different types of hydrodynamic boundary conditions at the surfaces of solids, drops and bubbles have been proposed. The appropriate choice will be dictated by experimental conditions. In this section, we shall only consider the *tangentially immobile*

boundary condition in which the fluid velocity at the film boundary is prescribed. For the axisymmetric head-on interactions considered here, this is equivalent to setting the tangential component of the fluid velocity to zero at the film boundary. In Section 4, we show that this boundary condition is consistent with results from a variety of experiments involving solids, drops and bubbles. The consideration of other types of boundary conditions will be deferred to Section 6.

3.2.1 Tangentially immobile interfaces. At the fluid–fluid interface of drops or the fluid–gas interface of bubbles with a constant interfacial tension, the conventional boundary conditions are that the tangential components of the fluid velocities and the shear stress are continuous, and the difference in the normal stresses across the interface is balanced by the Laplace pressure.[82] On the other hand, if the interface has a tangential surface tension gradient due, for example, to the presence of mobile surface-active species which have a non-uniform concentration along the interface, then this surface tension gradient will account for the difference in tangential shear stress across the boundary.[82]

The experiments in film drainage or dynamic interactions between deformable drops and bubbles surveyed in Sections 4 and 5 all involve head-on encounters that generate an axisymmetric lubrication flow in the radial direction in the film. The predicted time scales of the dynamics all turned out to be only consistent with the tangentially immobile boundary condition where the radial velocity vanishes, $u(r,z,t) = 0$, at the film boundaries: $z = 0$ and $z = h(r,t)$. In other words, although the interfaces of the drops and bubbles deform according to the Young–Laplace equation, the hydrodynamic boundary condition at these interfaces are like that at a "solid" surface. This observation is consistent across a variety of experiments and the most likely physical explanation is that such interfaces are immobilised by the presence of surface-active molecules.

With the tangentially immobile boundary condition, the solution of eqn (27) has the parabolic form:

$$u(r,z,t) = \frac{1}{2\mu}\left(\frac{\partial p}{\partial r}\right) z(z-h) \tag{29}$$

By combining this result with eqn (28), we have the Stokes–Reynolds equation for film drainage:

$$\frac{\partial h}{\partial t} = \frac{1}{12\mu r}\frac{\partial}{\partial r}\left(rh^3\frac{\partial p}{\partial r}\right) \quad \text{(tangentially immobile)} \tag{30}$$

We also note that with the tangentially immobile boundary condition at the fluid–fluid interface, any flow field inside the drop or bubble will not contribute to the film drainage process and so the internal viscosity of the drops or bubbles does not appear when this boundary condition is imposed.

The Stokes–Reynolds equation (eqn (30)) for tangentially immobile interfaces together with one of the augmented Young–Laplace equations (eqn (9), (14) or (16)) which we call collectively the Stokes–Reynolds–Young–Laplace (SRYL) equations completely describes the spatial and temporal evolution of the thin film between a drop and a flat surface or a particle or between two interacting drops. Of course, if boundary conditions different from the tangentially immobile condition were imposed, this would be reflected in the form of the Stokes–Reynolds equation (eqn (30)). These cases will be considered in Section 6.

Although the SRYL equations have been developed earlier,[7] being a set of coupled non-linear partial differential equations, they cannot be solved analytically although perturbation solutions for weak interactions have been developed.[83–85] Direct numerical solutions of the equations appropriate to drop–drop interactions in the four-roll mill are available[86] but due to the widely different length scales of the problem, very significant computational effort is required. Recently, an approach that combined boundary conditions specific to experimental setups together with a rapid and robust numerical algorithm has been developed to solve the SRYL equations and facilitate direct comparison with experimental data.[87] In Sections 4 and 5, we will undertake detailed comparison between the SRYL model and different types of experiments that measure deformations and forces.

There are other approximate solutions of the SRYL equations beginning with the classical Stefan–Reynolds model[19,20] that assumes the film trapped between deformed drops or bubbles can be approximated by a flat parallel disk of radius a. While this model gives a simple analytical solution, the film radius a is not known *a priori* and the model also predicts effects due to surface forces that are opposite to that observed in experiments (see Section 6.5 for detailed discussions). There are also numerous embellishments of the Stefan–Reynolds model with varying degrees of complexity and varying numbers of additional assumptions and parameters.[25,27] These models have been applied to a rather small number of simple experiments and none has been applied to account for a large number of experimental measurements of the spatial and temporal evolution of draining films.

3.2.2 Modelling different types of experiments. The Stokes–Reynolds–Young–Laplace equations, eqn (30) and (9), (14) or (16), together with eqn (7) for the force, completely determine the axisymmetric interaction and drainage of a thin film between deformable drops. As a system of coupled non-linear partial differential equations, they can only be solved numerically when the form of the disjoining pressure Π is specified. With appropriate initial conditions, these equations can be solved in the finite domain $0 < r < r_{max}$ together with boundary conditions at $r = 0$ and r_{max}.

We can impose the conditions $\partial h/\partial r = 0 = \partial p/\partial r$ at $r = 0$ because of axisymmetry. At $r \approx r_{max}$, we see from eqn (20)–(22) that the film thickness, h, contains a quadratic and a logarithmic term. Since according to the Young–Laplace equation the logarithmic term does not contribute to the pressure, p, and from the Stokes–Reynolds equation, a quadratic behaviour in h will contribute to a pressure that decays like r^{-4}, for $\partial h/\partial t \approx$ constant. This asymptotic behaviour of the pressure can be implemented as the condition: $r(\partial p/\partial r) + 4p = 0$ at $r = r_{max}$.

In most experiments, the drops at the initial distance of closest approach, h_o, are undeformed, so we can assume a locally quadratic drop shape with the initial film thickness of the form:

$$h(r,0) = \begin{cases} h_o + \dfrac{r^2}{2R} & \text{drop–wall} \\ h_o + \dfrac{r^2}{2}\left(\dfrac{1}{R} + \dfrac{1}{R_s}\right) & \text{drop–particle} \\ h_o + \dfrac{r^2}{\bar{R}} & \text{drop–drop} \end{cases} \quad (31)$$

The final condition is to specify how the drops are moved. For the drop–wall or drop–particle interaction, this can be found by differentiating the asymptotic results in eqn (20) or (21) with respect to time, t, and evaluate it at r_{max}:

$$\frac{\partial h(r_{max},t)}{\partial t} = \frac{dD(t)}{dt} - \frac{1}{2\pi\sigma}\frac{dF(t)}{dt}\left\{\log\left(\frac{r_{max}}{2R_o}\right) + B(\theta_o)\right\} \quad (32)$$

To model force measurement experiments using the atomic force microscope, we need to account for the deflection of the force sensing cantilever given by $S = F/K$, where K is the spring constant of the cantilever. With reference to the schematic diagram of the atomic force microscope in Fig. 5, we use the geometric condition: $D = S + X$ to eliminate D in eqn (32) in terms of the position, X, of the cantilever which can be controlled independently in the atomic force microscope. This gives the following boundary condition for the drop–wall or drop–particle interaction in AFM experiments:

$$\frac{\partial h(r_{max},t)}{\partial t} = \frac{dX(t)}{dt} - \frac{1}{2\pi\sigma}\frac{dF(t)}{dt}\left\{\log\left(\frac{r_{max}}{2R_o}\right) + B(\theta_o) - \frac{2\pi\sigma}{K}\right\} \quad (33)$$

For two interacting drops in the AFM, the boundary condition at r_{max} can be found in the same manner from eqn (22) to be

$$\begin{aligned} \frac{\partial h(r_{max},t)}{\partial t} = {} & \frac{dX(t)}{dt} + \frac{1}{K}\frac{dF(t)}{dt} \\ & - \frac{1}{2\pi\sigma_1}\frac{dF(t)}{dt}\left\{\log\left(\frac{r_{max}}{2R_{1o}}\right) + B(\theta_{1o})\right\} \\ & - \frac{1}{2\pi\sigma_2}\frac{dF(t)}{dt}\left\{\log\left(\frac{r_{max}}{2R_{2o}}\right) + B(\theta_{2o})\right\} \end{aligned} \quad (34)$$

Eqn (32)–(34) are conditions to be imposed at the boundary of the solution domain at $r = r_{max}$, of the inner problem as defined by the Stokes–Reynolds–Young–Laplace equations, namely eqn (30) with one of eqn (9), (14) or (16).

The way in which drops are driven enters *via* the prescribed functions dD/dt or dX/dt. The value of the force, $F(t)$, in these equations is obtained from eqn (7) by numerical integration. The disjoining pressure is negligible for $r > r_{max}$, but the contribution from the long-ranged nature of the pressure p should be included analytically using the r^{-4} dependence between $r_{max} < r < \infty$.

The boundary conditions in eqn (32) and (33) reflect the fact that we have already solved for the drop shape outside the interaction zone analytically by a perturbation method (see Appendix A) and then used this solution to provide a boundary condition for the inner problem at $r = r_{max}$. The force, $F(t)$, that appears in the boundary condition in eqn (32) and (33) depends on the motion and deformations of the drop that occurred at earlier times. Therefore, to completely determine the interaction between deformable drops it is important to have relevant initial conditions or past data. The term involving dF/dt has been omitted in earlier theoretical treatments of drop interactions[11,16,31] as these models were not concerned with modelling force measurement experiments.

The Stokes–Reynolds–Young–Laplace equations together with the boundary conditions in eqn (32) or (33) constitute a differential algebraic equation system. This can be solved numerically by the method of lines using standard software packages.[87] Since the film thickness may be down in the nm range while the domain r_{max} may be up to 100 μm, appropriate scaling of the equations is necessary for numerical robustness. Details of this scaling are given in Appendix B. As the scaled equations are nearly universal, some general and useful observations about the characteristics of dimple formation and film drainage rates are also given in Appendix B.

This completes the development of necessary theoretical background to understand and explain a broad range of experimental studies of film drainage and dynamic interaction involving drops and bubbles. In Sections 4 and 5 we will see how the model can be used to give quantitative explanations of results from measuring time dependent film deformations and forces involving drops and bubbles.

4. Dynamic deformations: experiments *vs.* theory

'*Both* (*theory and experiment*) *are worthless without a new original idea.*' I. B. Ivanov.[57]

In this section, we review measurements of time variations of the shape of draining films trapped between drops or between a drop and a flat surface. A variety of complementary experimental techniques were used and in many instances, results were presented originally without detailed comparison with theory. However, using the theoretical framework developed in Section 3 it is possible to account for such results with quantitative precision and without adjustable parameters.

4.1 Stable film: glycerol drops in silicone oil

The experiments we first consider correspond to the case of two identical drops that were driven together at constant velocity (detailed in Appendix B), in which opposing protuberant half drops of glycerol emerging from the ends of two sealed capillaries (3 mm diameter) in silicone oil 47V300 were used. The drops have an undeformed radius of $R_o = 1.52$ mm, interfacial tension $\sigma = 30$ mN m^{-1}, and subtend a contact angle $\theta = 90°$ at the capillary.[31,44] Careful alignment of the capillary axes ensured head-on interactions (Fig. 6). The drops were driven together from rest at an initial separation h_o, by propelling one capillary along the common axis towards the other at a constant velocity, $V = 6.7$ μm s^{-1}. With the instant $t = 0$ set to the time when the two drops would have touched if they did not deform, the drive was stopped at $t_{stop} = 27$ s. The spatial–temporal evolution of the profile of the film of silicone oil trapped between the glycerol drops continued after the drive has stopped and was recorded by filming the optical interference fringe pattern.

A comparison of experimental and theoretical fringe patterns predicted by the Stokes–Reynolds–Young–Laplace is given in Fig. 7 (inset). The film thickness profiles, $h(r,t)$, at times after the formation of the dimple deduced from the measured fringe

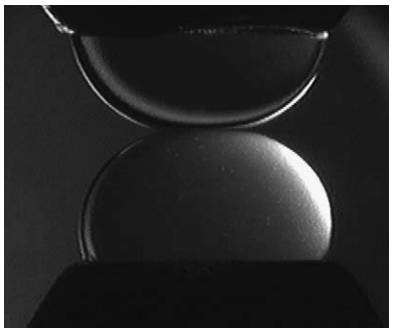

Fig. 6 Two interacting glycerol drops in silicone oil that have emerged from two opposing capillaries.

patterns are shown in Fig. 7 and compared against theory.[31,44] As the dimple first appears when the draining film is just over 5 μm thick, it is the long-range repulsive hydrodynamic pressure rather than the disjoining pressure that is responsible for the formation of the dimple. This occurs when the pressure in the film exceeds the Laplace pressure, $2\sigma/R_L \approx 40$ Pa for the glycerol drops in this experiment.

The agreement in both spatial and temporal variations of the fringe pattern or the film thickness, $h(r,t)$, without any adjustable parameters indicates that the Stokes–Reynolds–Young–Laplace (SRYL) equations with the assumption of tangentially immobile hydrodynamic boundary conditions at the drop interfaces has captured the physical behaviour of the system. The presence of trace impurities is likely to be responsible for the tangentially immobile boundary condition of the glycerol/silicone oil interface.

The same experimental setup has been used to study the interaction between two drops of aqueous solutions of polyethylene oxide (PEO) in a continuous phase of polydimethylsiloxane (PDMS).[129] Time dependent fringe patterns similar to those observed in glycerol drops in silicone oil were observed and these were consistent with dimpled films of thickness in the 1–2 μm range. Although no detailed comparisons of the film profile were made, it was clear that the rate of film drainage was again consistent with the tangentially immobile boundary condition. Given the presence of surface active PEO in the aqueous drop, this is not unexpected.

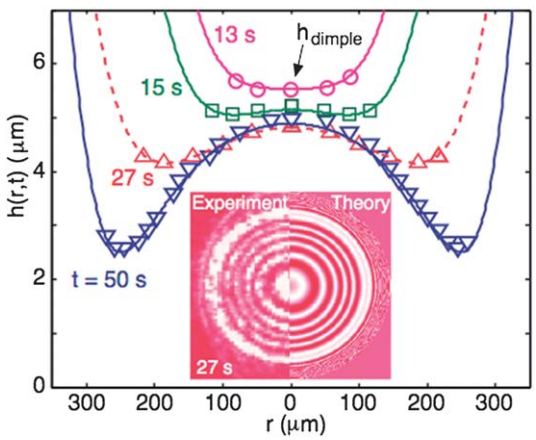

Fig. 7 Silicone oil film profile between glycerol drops at various times after the formation of the dimple: experiments (symbols) and theory (lines). Note the very different magnitudes of the vertical and horizontal scales. Inset: comparison of experimental and theoretical optical interference fringe patterns of the silicone oil film at $t = 27$ s when the capillary drive was stopped.

4.2 Stable film: bubble against quartz

Fisher *et al.*[2,29,30] used an optical interferometric technique to measure the evolving shape of a water film trapped between an expanding bubble against an optically flat hydrophilic quartz plate (Fig. 8). The protuberant bubble (unperturbed radius 1.16 mm), at an initial distance of closest approach of 40 μm from the quartz plate, was expanded rapidly from an orifice (diameter 2 mm) in a fraction of a second. The shape of the trapped water film that subsequently drained before reaching a stable film was measured. The final equilibrium film was stabilised by electrical double layer repulsion between the quartz surface and the bubble. Depending on the concentration of added electrolyte, the drainage process could last over 200 s.

As the bubble was expanded rapidly in a fraction of a second, the subsequent drainage process took place under a constant applied force.[41] Although this constant force is not known *a priori* in the experiment, its magnitude can be deduced from the final shape of the stable film together with the surface potential of the quartz and bubble surface that determine the repulsive electrical double layer repulsion.

In Fig. 9, we compare the experimental results of Fisher *et al.*[2] with predictions of the full Stokes–Reynolds–Young–Laplace model for film drainage in distilled water. This experiment gave the thickest equilibrium film. Comparisons with results at higher salt concentrations are equally good.[52] The theoretical results were obtained with no adjustable parameters.

The change in Laplace pressure of the deformed bubble in these experiments was small. For the case in distilled water, the pressure changed from 124 Pa to 132 Pa upon expansion, and drainage took place under an applied force of 43 μN over an interaction zone of radius ~360 μm.

By increasing the salt concentration, the double layer repulsion is decreased and the equilibrium film will be thinner. However, the drainage of the dimpled film is controlled by the film thickness, h_{rim}, at the barrier rim. Thus at higher electrolyte concentrations, h_{rim} is smaller and therefore the dimple takes longer to drain.[52] In contrast, the Stefan–Reynolds parallel film model

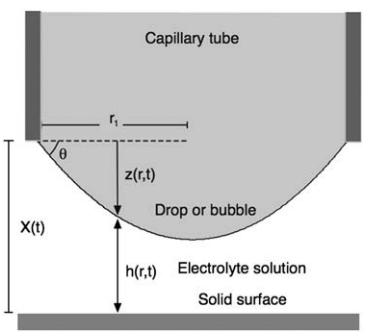

Fig. 8 Schematic diagram of a protuberant drop or bubble that has emerged from a capillary against a flat solid surface.

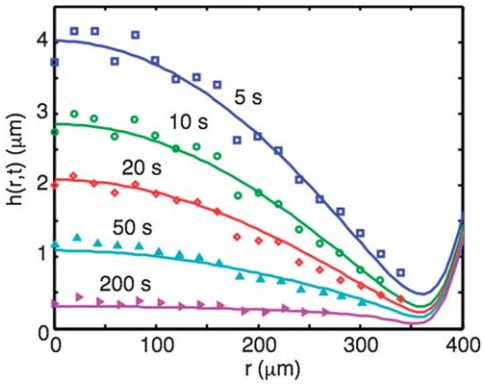

Fig. 9 The axisymmetric shape of the draining water film thickness, $h(r,t)$, as a function of position, r, between a bubble and a quartz plate in distilled water ($\sim 2 \times 10^{-6}$ M NaCl).

predicts that drainage is faster at higher salt concentrations—opposite to experimental observations.[52] See also Section 6.5.

The tangentially immobile hydrodynamic boundary condition was applied at the quartz and bubble surfaces. While this is a reasonable boundary condition for the quartz–electrolyte interface, the reason why this is also required at the bubble surface is not certain. What is clear is that any other hydrodynamic boundary condition at the bubble surface would result in the water film draining too fast compared to experimental observations.

Interestingly, a recent experiment that measured the rate of rise and approach of microbubbles (diameters < 100 μm) in ultra clean water towards a hydrophilic titania (TiO_2) plate also indicated that results are consistent with the tangentially immobile boundary condition at the bubble surface.[62,63] This is unexpected because the measured terminal velocities of such rising bubbles follow the Hadamard–Rybczynski formula that corresponds to a fully mobile bubble interface[88] (see also Section 6.4). A possible explanation of such apparently contradictory observations may be attributed to trace surface-active contaminants that accumulate at the bubble surface as they approach a solid surface in spite of extreme care taken in cleaning the water. Only trace amount of such accumulated surfactants, sufficient to lower the bubble interfacial tension by 0.1 mN m^{-1}, a variation that is difficult to detect, is sufficient to give rise to a tangentially immobile interface.[45,46] However, a definitive explanation has yet to be found.

4.3 Stable and unstable films: mercury against mica

The Surface Force Apparatus had been adapted to measure the time evolution of the shape of the aqueous electrolyte film trapped between a mercury drop and an approaching or receding molecularly smooth mica surface[33,34] (Fig. 8). By observing Fringes of Equal Chromatic Order (FECO) it was possible to resolve the film thickness with sub-nanometre precision. Mercury was selected for its deformability, known interfacial tension and for its high optical reflectivity that facilitated the formation of sharp fringes. Being a perfectly polarising fluid, its surface potential could be controlled independently to give repulsive as well as attractive electrical double layer disjoining pressures that allowed the evolution of stable and coalescing films to be investigated. The material properties used were well defined so such experiments provided detailed and information-rich benchmark results of the film drainage mechanism.

The changing film shape was measured by video recording of the FECO fringes with subsequent conversion to film thickness profiles. In Fig. 10, we compare the time evolution of the drainage of an axisymmetric aqueous electrolyte (0.1 mM KCl) film trapped between the mercury drop and the approaching mica plate moving with velocity 24 μm s^{-1} for a time and then stopped. When the mercury drop was held at a negative surface potential,[34,41] the drop surface developed a dimple and the electrical double layer repulsion between the drop and the negative mica plate was responsible for an equilibrium film of about 90 nm thick. The final 14 s of the evolution of the film profile is shown in Fig. 10a. With the mercury held at a positive potential that gave a double layer attraction, the mercury rapidly jumped into contact with the mica plate in about 0.6 s as shown in Fig. 10b. The coalescence mechanism is *via* a rapid axisymmetric thinning of the barrier rim although eventually this symmetry is likely to be broken at the very final moments of coalescence.

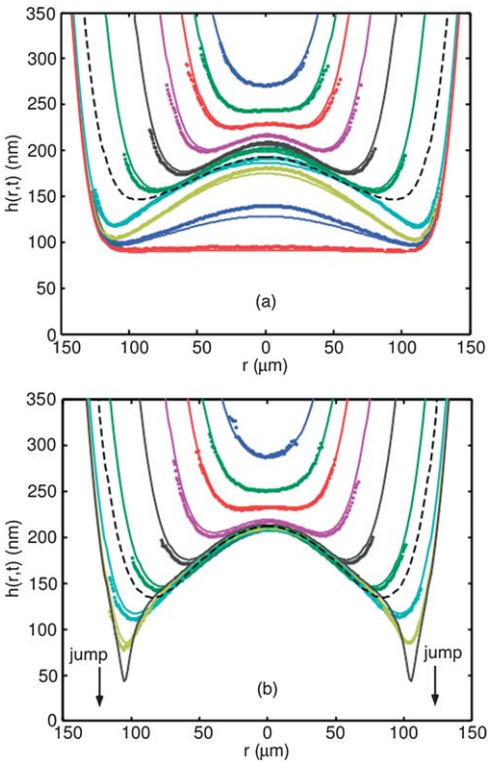

Fig. 10 Time evolution of the thickness of the aqueous electrolyte (0.1 mM KCl) film trapped between a mercury drop and a negatively charged mica plate as it approaches at 24 μm s^{-1}.[41] The profile drawn in broken line indicates the time at which the mica plate stopped. The disjoining pressure due to electrical double layer interaction is (a) repulsive with a negative mercury surface potential that resulted in an equilibrium film in a time interval of 14 s as shown and (b) attractive with a positive mercury surface potential that resulted in coalescence over a time interval of 0.6 s as shown. Note the very different magnitudes of the vertical and horizontal scales.

After the mica plate stopped, at the times indicated by the broken curves in Fig. 10, the film continued to drain under a constant force constraint because there was no further external displacement in the system. The force calculated according to the Stokes–Reynolds–Young–Laplace model was consistent with this expectation[41] (see also Fig. 12).

The key lessons in this comparison is that the Stokes–Reynolds–Young–Laplace model together with electrical double layer interactions calculated using the full Poisson–Boltzmann model gave good quantitative agreement using input parameters (*e.g.* interfacial tension, surface potentials) that can be measured independently. There are no free parameters in the model. The coalescence mechanism is what would be expected from the Derjaguin–Landau–Verwey–Overbeek (DLVO) theory of colloidal stability but with allowance for interfacial deformability. There is no need to invoke thermal fluctuations in the film thickness to initiate coalescence.[21] Furthermore, for coalescing films, the assumption of the Stefan–Reynolds parallel film geometry becomes progressively less realistic.

Again we observe that the drainage rates of both stable and coalescing films are consistent with the tangentially immobile boundary condition at the mercury–electrolyte interface although a physical mechanism that gives rise to this boundary condition is not immediately apparent.

4.4 Transient behaviour: mercury against mica

The ability to move the mica plate independently in close proximity to the deformable mercury drop affords the opportunity to investigate complex transient behaviour of deformable drops and bubbles. Starting with the initial state of an equilibrium aqueous film that had been stabilised by double layer repulsion, the mica plate was displaced rapidly over a short time period further towards the drop. Clearly, the final state would be an equilibrium film of the same thickness, but with a larger radial dimension as the mercury had been compressed further. The question we ask is: what are the intermediate shapes of the deformable mercury drop and of the aqueous film during the transition from the initial to the final state under such a mechanical perturbation?

The experimental results[37] and predictions of the Stokes–Reynolds–Young–Laplace model[42] are shown in Fig. 11. The transition from the initial flat film is shown in Fig. 11a and the approach to the final of the same thickness, but of larger radial dimension, is shown in Fig. 11c. The novel behaviour of this axisymmetric film is the transient 'wimple' shape—middle curve in Fig. 11b, which exhibits a local maximum and a local minimum in thickness in addition to the local minimum at the axis of symmetry, $r = 0$. It is also interesting to note that the film thickness at the axis of symmetry, $r = 0$, first *increased* as the mica was displaced towards the mercury drop (Fig. 11 a and b) before returning to the equilibrium value in Fig. 11c.

There are other attempts to model this experiment using the same differential equations. However, either the boundary conditions chosen were unrelated to the experimental situation[89,90] or an inappropriate one-dimensional scaling metric for a Taylor bubble was used for the actual axisymmetric problem.[71] Therefore any agreement between such theories and experiments is at best, qualitative.

A second transient experiment involved pushing the mica plate towards the mercury drop under a repulsive double layer disjoining pressure, waiting for the equilibrium film to establish and then rapidly pulling the mica surface away from the flattened mercury drop. In Fig. 12, we show the experimental and theoretical time variations of the central thickness, $h_o(t) \equiv h(r = 0,t)$, of the axisymmetric aqueous film, as well as the rim thickness, $h_{rim}(t) \equiv h(r_{rim},t)$, when it can be identified after the formation of the dimple (see also Fig. 1). Note the changes in scale of the time axis.

Salient features of the sequence of transient behaviour in this push–pull experiment are highlighted in Fig. 12. After dimple

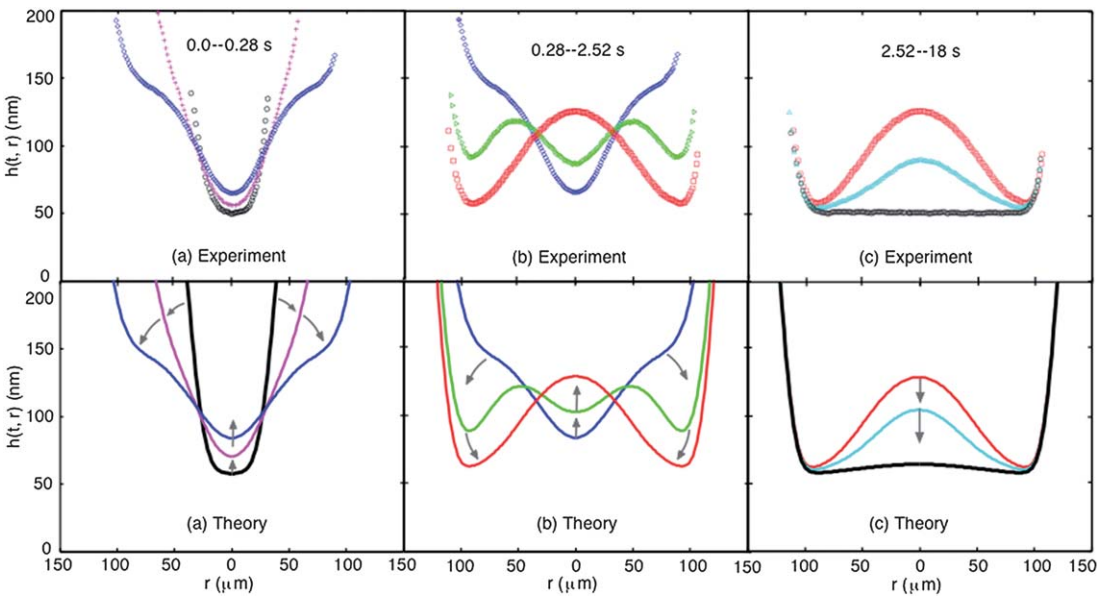

Fig. 11 Wimple: the transient shapes between two equilibrium aqueous electrolyte (1 mM KCl) films generated by a rapid displacement of the mica plate towards the mercury drop according to experiments (symbols) and theory (lines). Arrows indicate the progression of time: (a) the initial shapes of the film, 0.0–0.28 s, (b) the intermediate shapes including the wimple, 0.28–2.52 s and (c) the approach to the final state, 2.52–18 s.

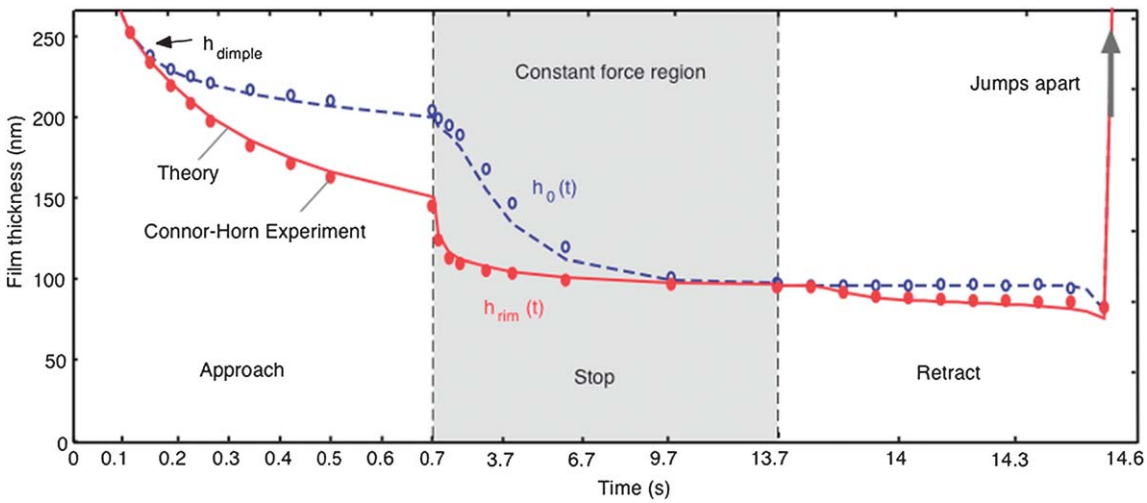

Fig. 12 Comparison of the measured and predicted film thickness of electrolyte (0.1 mM KCl) between a mica plate and a mercury drop at the centre of the film, $h_o(t)$, and at the rim of the dimple, $h_{rim}(t)$. The mica was driven towards the mercury drop at 24 μm s^{-1} until 0.7 s after the formation of a dimple and was then stopped for 13 s before it was rapidly retracted from the drop.

formation that occurred at around 0.15 s, the mica plate was stopped at 0.7 s and the system continued to evolve under constant force until the establishment of a flat equilibrium film at around 10 s as indicated by $h_o(t) = h_{rim}(t)$. At 13.7 s, the mica plate was pulled away rapidly from the mercury drop and they jumped apart to a large separation at around 14.5 s. Unlike expectations for rigid systems, the central separation, $h_o(t)$, actually decreased as the mica plate was pulled away from the mercury drop. This novel behaviour was the response of the deformable drop to the negative hydrodynamic pressure generated by the retraction of the mica plate. This is similar to the suction one experiences while attempting to lift a wet glass off the table.

These complex transient responses are predicted with quantitative accuracy by the Stokes–Reynolds–Young–Laplace model. They are also consistent with coalescence on separation between two drops in another liquid under shear flow conditions between parallel plates.[91] It was also observed in a four-roll mill setup, when the drops were driven slightly off-centre where they would rotate alongside each other and coalesce in the extensional quadrant.[92–94] Avalanches of coalescence events[95] were also observed experimentally and could be associated with this separation effect.

Perturbation solutions of the Stokes–Reynolds–Young–Laplace equations do indeed offer a hint of the above experimental observations[83,84] and also corrected a flawed explanation[85] of drop coalescence upon separation in a microfluidic channel.[96] However, quantitative agreement with the observed transient response of the film requires the (numerical) solution of the nonlinear SRYL equations with the correct boundary conditions.

4.5 Scheludko cell experiments

One of the earliest studies of the film drainage mechanism was based on the Scheludko cell.[18] The basic operation of the cell is illustrated in Fig. 13. A drop of solution is placed in a cylindrical cell of diameter in the millimetre range. To model the interaction between two drops or bubbles, both ends of the cell are filled with

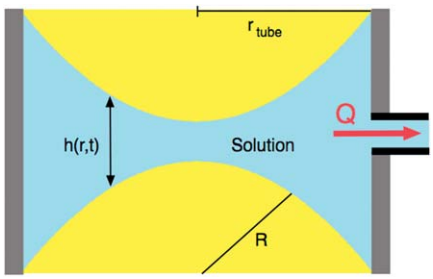

Fig. 13 Schematic diagram of the Scheludko cell.

a second liquid or gas phase. The central solution is then withdrawn from the cell at some volumetric rate Q and the resulting thinning of the film of solution between the two "drops/bubbles" is observed by optical interference. A very large body of literature comprising original papers and review articles of experimental work and theoretical models has accumulated over the past half-decade around this technique.[18,21–23,28,48,49]

In principle, it is possible to obtain the time evolution of the entire film profile, $h(r,t)$, as in experiments described earlier in this section. In practice, only the time variation of the "average" film thickness is reported and such results are then only analysed in terms of the Stefan–Reynolds Flat Film Model (see Section 6.5) or its later variants. It is unfortunate that important and informative experimental data relating to the drainage process observed using the Scheludko cell have not been recorded or reported to allow comparison with theories not based on the Stefan–Reynolds Flat Film Model.

With one exception[97,98] the physical content of various attempts at modelling drainage in the Scheludko cell are less than physically perspicuous as increasingly complex assumptions are made and esoteric mechanisms are added to remedy the inherent limiting assumptions of the Flat Film Model. Furthermore, these complex models have not been applied to account quantitatively for any of the experimental results that have not been obtained using the Scheludko cell.

Therefore, although the Scheludko cell was a pioneering experiment technique in the field and had stimulated the

development of a number of theoretical models, the deployment of experiment and theory has not yet been sufficiently general to exploit their full potential.

5. Dynamic forces: experiments and theory

The understanding of nanoscale interactions and stability to macroscale static and transport properties of emulsions and particulate systems has long been based upon the consideration of equilibrium interactions. Only in the past decade have direct dynamic force measurements on the nanoscale been extended to particles and drops in relative motion. The combined consequences of hydrodynamic interactions, deformation of soft materials and molecular transport have given rise to fundamental questions that remain unexplored.

In this section, we review recent developments in direct force measurement involving deformable drops and bubbles in relative motion using the atomic force microscope (AFM). These experiments require novel techniques to generate, capture and accurately place drops and bubbles of ~100 μm diameters on substrates and on force sensing micro-cantilevers.

Time varying changes in geometries associated with deformations during the interaction process require a cognate theoretical framework to interpret the measurements. In the previous section, we saw that such a theoretical framework is able to account for detailed measurements of dynamic deformations. In this section, we review recent results of dynamic force measurements that complement such dynamic deformation studies.

Dynamic force measurements using the AFM can be regarded as studying controlled collisions between two drops. With a drop positioned on the substrate and accurately aligned to another drop anchored on one end of the force sensing micro-cantilever, the axisymmetric collision is driven by changing the cantilever displacement, $X(t)$, of the other end using a piezo electric motor (see Fig. 5). From an initial position where the colliding drops are far apart, $X(t)$ is first decreased in the approach phase for a set time interval at a nominal speed and then increased in the retraction phase at the same or different speed. This is termed an approach–retract cycle. Variations of this collision protocol may be an approach–stop or approach only drive without retraction.

The time dependent force, $F(t)$, can be deduced from the cantilever deflection detected using a light lever together with the spring constant of the cantilever that is determined independently. The nature of dynamic forces and the robustness of any theoretical model can be probed by varying experimental variables such as the nominal approach and retraction speeds, the maximum displacement of the cantilever and the initial starting position.

As all physical parameters of the system can be measured independently, at least to within experimental tolerance, there are no free parameters available to match experiments and theory. Consequently, there is confidence in using such a theoretical framework to infer physical attributes or mechanisms that may not be easy to measure directly.

5.1 Stable drops: hydrocarbon drops in water

The theoretical basis for analysing AFM measurements between two drops is embodied in the Young–Laplace equation (eqn (16)) for interfacial deformation due to hydrodynamic and disjoining pressures and in the Stokes–Reynolds model, eqn (30), for fluid flow in the thin film between the two drops. In eqn (30) the interfaces are assumed to be tangentially immobile in their hydrodynamic response. The collision between two drops as a function of time, t, is specified by the cantilever displacement function $X(t)$ (see Fig. 5) that enters as a boundary condition, eqn (33), for the Stokes–Reynolds–Young–Laplace equations. Eqn (7) gives the time dependent force, $F(t)$.

In Fig. 14, we show a comparison between the time dependent force measured using the AFM[40] and predictions of the Stokes–Reynolds–Young–Laplace model between two decane drops in aqueous electrolyte. The drops with radii 43 μm and 90 μm were driven at different nominal cantilever speeds for an approach–retract collision. Sodium dodecyl sulfate (SDS) was also present at a concentration of 3 mM to ensure that the decane/electrolyte interfacial tension was a known quantity and would not be affected by possible trace contamination. The surface potential of the SDS populated oil/water interface was also known which allowed the disjoining pressure due to electrical double layer repulsion to be determined.

For each drive speed, the total cantilever displacement was the same so that the time axis can be scaled by the total time, t_{total}, of a single approach–retract collision. The thermal Brownian velocities of emulsion drops of comparable sizes (~7 μm s^{-1}) fall within the range of drive speeds used.

At low drive speeds (2 μm s^{-1}) there is near symmetry between the approach branch ($0 < t < \frac{1}{2}t_{total}$) and the retract branch ($\frac{1}{2}t_{total} < t < t_{total}$) of the force curve (Fig. 14). With increasing drive speeds, the velocity dependent force became significantly more repulsive on approach due to hydrodynamic repulsion as water had to be displaced from between the approaching drops. Near the start of the retraction phase, the force rapidly became attractive with a deeper minimum at higher speeds. The development of the attractive minimum was again due to hydrodynamic suction as upon separation water had to be drawn in to fill the thickening film between the separating drops. As the hydrodynamic force between two rigid particles would become negative as soon as the cantilever motion changes from the

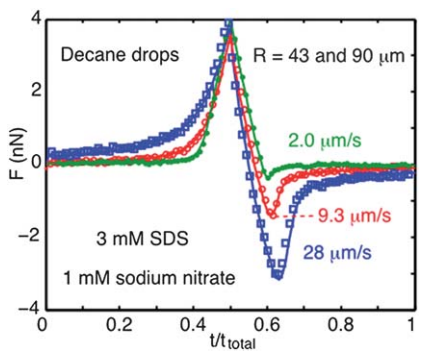

Fig. 14 The time dependent force between two decane drops (radii 43 μm and 90 μm) in 3 mM SDS and 1 mM $NaNO_3$ aqueous electrolyte, at nominal approach and retraction velocities 2.0, 9.3 and 28 μm s^{-1}. Time is scaled by the total collision time, t_{total}, over a cantilever displacement amplitude of 2 μm.

approach phase to the retraction phase, the rounded shape of the hydrodynamic minimum was a signature of the ability of the drops to deform.

The height of the force maximum depends on the combined value of the initial separation between the drops and the total displacement of the cantilever which in turn determines the extent that the drops have been pushed together and the extent of drop deformation.

5.2 Drop–particle interactions and viscosity effects

By replacing the drop on the cantilever with a silica microsphere, the same atomic force microscope setup can be used to measure the force between a particle and a drop. The general features of the force curves are similar to the two drops case considered in Section 5.1 if there is no coalescence between the particle and the drop.

Such particle–drop systems have been used to study the effects of viscosity of the continuous phase on the dynamic force.[50] Results for the driven collision between a silica microsphere (radius 12 μm) and a tetradecane drop (radius 107 μm) in aqueous sucrose solutions of varying concentrations with 5 mM SDS are shown in Fig. 15. The dynamic force is shown as a function of the cantilever displacement at a speed of 1 μm s^{-1}. The addition of up to 40% by weight of sucrose can increase the viscosity of the Newtonian aqueous solution by almost 6-fold.

As expected, increasing the viscosity had a similar effect to increasing the drive speed of the collision. With no added sucrose, only a very small hysteresis in the force curve was evident. As the viscosity of the continuous aqueous phase was increased an attractive hydrodynamic attraction began to develop on the retraction branch.

Another informative feature of the results in Fig. 15 is the illustration of the utility of the force–displacement formula (24) which in the present context can be re-cast in the following form since $\Delta X(t)$ is arbitrary up to an additive constant:

$$\Delta X(t) \cong \frac{F(t)}{4\pi\sigma}\left\{\log\left(\frac{F(t)R_{ds}}{8\pi\sigma R_o^2}\right) + 2B(\theta_o) - \frac{4\pi\sigma}{K} - 1\right\} \qquad (35)$$

Predictions of this approximate analytic result are shown as broken lines in Fig. 15. At modestly high forces when the approach and retraction portion of the force curves overlap, this analytic formula gives excellent agreement with experiments. Being a quasi-static result, it is independent of viscosity as evident in Fig. 15. The result in eqn (35) replaces the constant compliance condition for rigid particles in contact and also illustrates that the response of the deformable drop is not Hookean since the force, $F(t)$, is clearly not proportional to the displacement, $\Delta X(t)$.

The theoretical model that is used to model experimental results in Fig. 14 and 15 assumed the decane or tetradecane interface is tangentially immobile. This is entirely expected in the presence of added SDS surfactant that would arrest interfacial flow. With the tangentially immobile boundary condition, there is no need to consider viscosity ratios of the drop to the continuous phase as this boundary condition decouples flow outside the drop to any possible flow inside the drop.

In Fig. 16 we show a comparison of the time dependent force between experiment and theory around the initial rise of the approach branch and around the attractive minimum on the retraction branch at two different drive speeds.[47] The entire force curve at a drive speed of 23 μm s^{-1} is shown as an inset.

The quantitative difference in the force curves between the results in Fig. 14 for two oil drops (radii 43 μm and 90 μm) and Fig. 16 for between an oil drop (radius 55 μm) and a microsphere (radius 12 μm) is in the magnitudes of the attractive minima at comparable drive speeds. Even though the oil drop in the particle–drop experiment can deform, the small fixed size of the microsphere reduced the effective area of interaction, because for two interacting drops, both drops can deform to increase the effective area of interaction.

As an illustration of drop deformation around the microsphere, we show in Fig. 17, the shape of the deformed drop as well as the thickness of aqueous electrolyte trapped between the particle and the drop. This film was stabilised by electrical double

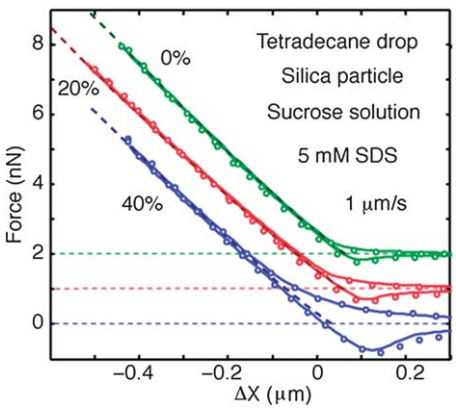

Fig. 15 Viscosity effects on the force between a tetradecane drop and a silica particle as a function of cantilever displacement at 1 μm s^{-1} in sucrose solution of varying concentration in wt% with 5 mM SDS: experiments (symbols) and theory (solid lines). For visual clarity, the zero force datum line at different sucrose concentrations have been displaced vertically. Results according to the high force formula in eqn (35) are shown as broken lines.

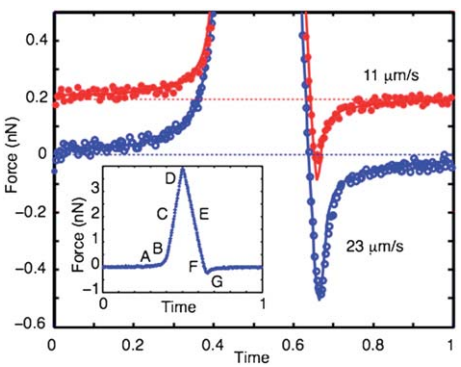

Fig. 16 Close up view of the force minimum between a silica microsphere (radius 12 μm) and a tetradecane drop (radius 55 μm) at two different nominal drive speeds: experiments (symbols) and theory (solid lines). The time axis is scaled by the total collision time. Inset: force *versus* time curve at a nominal drive speed of 23 μm s^{-1}. See Fig. 17 for an explanation of the points labelled A to G.

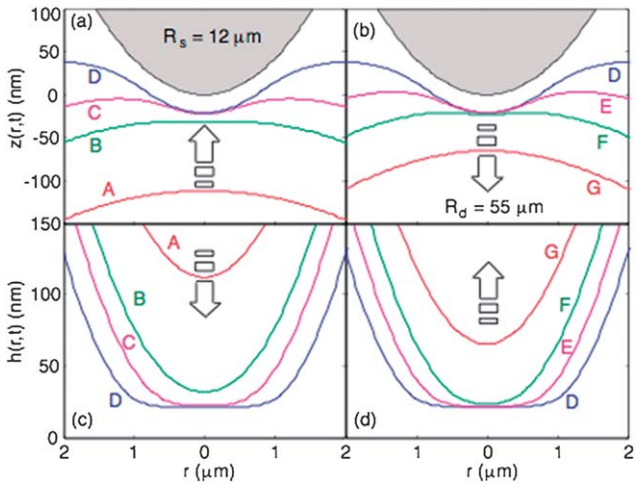

Fig. 17 Theoretical results for a tetradecane drop (radius 55 μm) interacting with a silica microsphere (radius 12 μm) at a drive speed of 23 μm s^{-1}. The panels show the calculated drop shape (a) on approach and (b) on retraction and the calculated aqueous film thickness, $h(r,t)$, during the (c) approach and (d) retraction phase. The large arrows indicate the directions of motion of the interface. The labels A to G correspond to time points marked in the inset of Fig. 16.

layer repulsion between the microsphere and the oil drop that were both negatively charged. This repulsion determines the thickness of the water film as the oil drop wrapped around the microsphere near the force maximum (curve D in Fig. 17a and b).

5.3 Coalescence: bubble–bubble

The outcome of bubble–bubble collisions determines the efficacy of bubbles as contrast agents in medical ultrasonic imaging to the delivery of flavour and sensation in soft drinks and champagne. The coalescence of two bubbles or gas voids in water is perhaps the simplest interacting system that one can study. Surprisingly, the idea of driving two bubbles together or separating them in a well controlled and characterised manner while measuring directly the dynamic force between them has only been attempted with quantitative success recently.[51] Such experiments can also reveal the varied and sometimes unexpected conditions under which coalescence can take place.

Three different collision modes were used to study bubble collision and coalescence using the atomic force microscope. Ultrasonic generated bubbles of radii in the 50–100 μm range in aqueous electrolyte (0.5 M $NaNO_3$) were used. One bubble was mounted on the substrate and the other anchored at one end of a rectangular force-sensing cantilever.[51] The other end of the cantilever was driven towards the substrate at a nominal speed of ~50 μm s^{-1}. In this case of continual approach, the repulsive force between the bubbles increased monotonically with time. For two bubbles with radii 62 μm and 86 μm and initial separation of 5.5 μm, such an "Approach only" force curve is shown in Fig. 18a. We see that the bubbles coalesced when the force reached about 150 nN. In a second similar experiment, the cantilever was driven towards the substrate at the same nominal speed but was then stopped while the force between the bubbles continued to evolve. The force corresponding to such an "Approach–Stop" collision between bubbles with radii 67 μm and 85 μm and initial separation

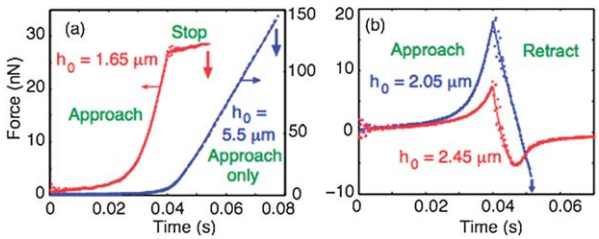

Fig. 18 The time dependent force between two bubbles (radius 50–70 μm) during collision events at a nominal drive speed of ~50 μm s^{-1} in 0.5 M $NaNO_3$ aqueous electrolyte: experiments (symbols) and theory (solid lines). The results of three collision protocols are shown: (a) Approach only and Approach–Stop, and (b) Approach–Retract for the same bubble pair at different initial separations, h_o. The coalescence time is indicated by the downward pointing arrows.

of 1.65 μm, is shown as the "Approach–Stop" curve in Fig. 18a. Note that after the cantilever stopped, the bubbles continued to evolve under an almost constant force condition (~27 nN) before coalescence eventually occurred.

The third mode of collision involved driving the cantilever towards the substrate at the same nominal speed for a fixed time and the cantilever is then retracted at the same nominal speed. The outcome of such an "Approach–Retract" collision depended rather sensitively on the initial separation. For a pair of bubbles with the same radius (74 μm) at an initial separation of 2.45 μm, the dynamic force (Fig. 18b) attained a maximum of about 8 nN and then decreased during the retraction phase and reached an attractive minimum of about 6 nN in magnitude before separating eventually. Thus this collision is stable as the bubbles did not coalesce and the force curves are similar to those seen between two oil drops (Sections 5.1) and between a particle and an oil drop (Section 5.2). However, repeating the experiment with the same bubble pair, but starting at smaller initial separation of 2.05 μm, the force reached a larger repulsive maximum of about 18 nN (Fig. 18b) and then decreased during the retraction phase. But instead of reaching some attractive minimum as in the previous Approach–Retract collision, the bubbles coalesced—while they are being separated.

In Fig. 18, the experimental data are shown in points and the predictions of the Stokes–Reynolds–Young–Laplace model, shown as lines, only included the attractive Van der Waals contribution to the disjoining pressure. Electrical double layer interactions are negligible in a 0.5 M $NaNO_3$ solution. Although no surfactants were added and Millipore water of specific resistance in excess of 18.3 MΩ cm were used, once again, the experimental force data were consistent with predictions using the tangentially immobile boundary condition for these two bubble interactions.

In Fig. 19, we show observed experimental coalescence times obtained from 30 different trials on the AFM from the three collision modes of Approach only, Approach–Stop and Approach–Retract.[51] These are compared against predicted values from the Stokes–Reynolds–Young–Laplace model. The quantitative agreement is quite satisfactory and suggests that the postulated mechanism of coalescence being initiated by thermally excited surface fluctuations[21] does not play a role in these experiments.

Since the Stokes–Reynolds–Young–Laplace model gave good quantitative predictions for the dynamic force and coalescence

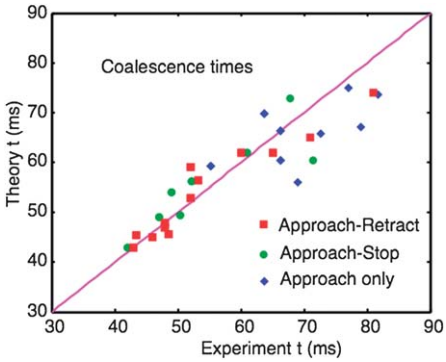

Fig. 19 A comparison of experimental and predicted coalescence times for the three different collision protocols. The time $t = 0$ is defined as the instant when the bubbles are 1.5 μm apart.

times, we can, with some confidence, use the model to predict the dynamics of surface deformations of the bubbles during interaction. An example of this is given in the animation video in the ESI† where the evolution of the film velocity, $\partial h(r,t)/\partial t$, is shown for the case of the stable Approach–Retract collision given in Fig. 18b. The two salient features to note are that (a) when the force, F, between the drops is zero during the retraction phase (see inset in Fig. 20a), the quantity $\partial h(r,t)/\partial t$ is negative (shown in red in Fig. 20a), that is the film is thinning in the central portion of the film for small r, but at the same time, $\partial h(r,t)/\partial t$ is positive, that is the film is thickening, in the outer part of the film at large r (shown in blue in Fig. 20a and b) after the attractive minimum of the force curve (see inset in Fig. 20a), the thickness of the central portion of the film at small r increases faster than or "overshoots" the retraction speed before the bubbles finally separate (see Fig. 20b). Note that such behaviour occurs within the low Reynolds number, Stokes flow regime and comes about because the model took into account the effects of bubble deformation and pressure variations in the deformed thin film in a consistent way.

6. Other theoretical considerations

In our review of experiments thus far, all examples of film drainage and dynamic interactions involving drops and bubbles appear to be consistent with the tangentially immobile hydrodynamic boundary condition at the deformable interfaces. However, there is a large body of theoretical models of interacting drops and bubbles that consider other boundary conditions. These will be summarised in this section with comments as to their role in modelling experimental measurements.

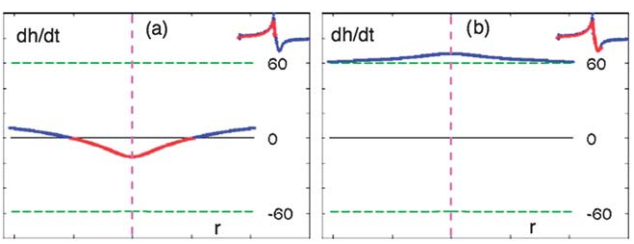

Fig. 20 Velocity of the bubble surface, $\partial h(r,t)/\partial t$, with the force, $F(t)$, in the inset, as the bubbles are driven together and then separated at a nominal speed of 50 μm s^{-1} at: (a) the instant when the dynamic force, $F = 0$, during the retraction phase and (b) just after the force minimum. An animated movie file is available as ESI.†

6.1 Remarks on hydrodynamic boundary conditions

6.1.1 Solid–liquid interfaces. In formulating the Stokes–Reynolds equations that govern the axisymmetric film drainage in Section 3.2.1 we have imposed the tangentially immobile hydrodynamic boundary condition at the liquid–liquid and bubble–liquid interfaces. This condition is equivalent to specifying the fluid velocity at the interface. For radial lubrication flow in the film drainage problem, the dominant tangential fluid velocity is set to zero at the interface. This boundary condition is equivalent to that applied normally at a solid surface—commonly referred to as the "no slip' condition, although we do allow the fluid–fluid interface to undergo deformation according to the Young–Laplace equation under the combined influence of hydrodynamic and disjoining pressure.

The choice of the hydrodynamic boundary condition is determined by flow conditions and transport processes that prevail at the interface. Historically, this issue was a subject of intense debate at the time when the Navier–Stokes continuum description of fluid mechanics was first formulated.[99,100] Navier[101] proposed that the tangential component of fluid velocity at a solid boundary may be proportional to the tangential shear stress, with the constant of proportionality being the slip length, b (Fig. 21a). But following an investigation commissioned by the Royal Academy of Science, the "no slip" boundary condition at a solid–liquid interface was adopted after considering experimental results from different quarters.[99]

Towards the end of the last century, there was a resurgence of interest in the phenomenological Navier model as a way to allow the boundary condition at a smooth solid surface to deviate from the familiar no-slip condition. The origin of this can be traced to an assertion[102] that the boundary condition for the flow of water

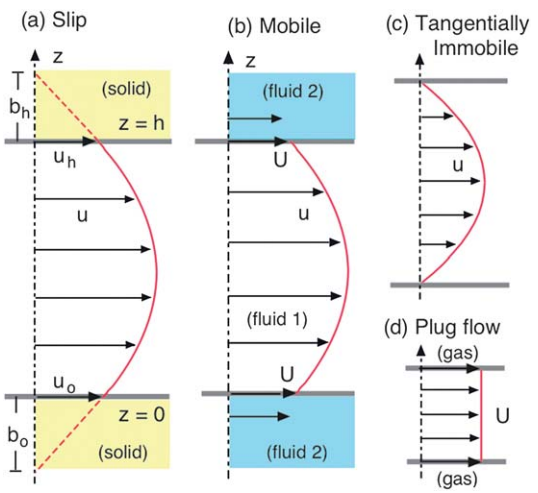

Fig. 21 Schematics velocity profile, u, for various boundary conditions: (a) Navier slip at solid surfaces with slip lengths b_o and b_h, (b) mobile interfaces between different fluids with surface velocity U, (c) tangentially immobile interfaces and (d) plug flow between interfaces.

at smooth hydrophobic surfaces obeys the Navier slip condition. Although the magnitude of the slip length was not predicted or specified in this model, an unrealistically large slip length of 1 μm[103] was needed to match what was attributed to "hydrophobic attraction" observed using the Surface Forces Apparatus. In reality, surfaces that are deemed hydrophobic can be rather complex. In some hydrophobic surfaces, bubbles nucleate and populate such surfaces[104] while other examples of hydrophobic surfaces may have complex surface geometries that impart the characteristic hydrophobic properties.[105] Therefore it is not informative to subsume such interfacial complexities using a model with a mathematically smooth surface that has a slip length as a fitting parameter.

Interest in flow in microfluidic geometries also prompted renewed questions about the validity of the "no-slip" boundary conditions for flow in confined geometries down to the nanometre regime. There are a number of reports of observed deviations from Stokes flow with the "no-slip" boundary for Newtonian fluids at "smooth solid" surfaces.[106–108] However, as such experiments were based on dynamic force measurements between a microsphere probe and a flat solid surface on the atomic force microscope, the conclusions depend critically on the accurate location of the solid–liquid boundaries. A recent careful re-evaluation of such measurements suggests that the slip length, b, for water in such systems is close to zero: $b \approx 1\ \text{nm} \pm 1\ \text{nm}$, within experimental tolerance and indistinguishable from the "no-slip" boundary condition.[109,110] Moreover, as the magnitude of the slip length is dependent on the type of the force sensing cantilever used in the measurements[111] it is not possible to rule out entirely the effects of technical artefacts in the phenomenon of slip observed using the atomic force microscope.

6.1.2 Fluid–fluid interfaces. The physical processes that give rise to different hydrodynamic boundary conditions at the interface between two Newtonian fluids are well known.[82] If the interface is ideal in the sense that there are no mechanisms present at the interface to sustain tangential stress, the boundary condition at such interfaces will be the continuity of the tangential components of the fluid velocities and the tangential shear stress across the interface. This follows from kinematic and force balance considerations.[82] In Section 6.3 we give the film drainage equations for this case that will replace eqn (30) for the tangentially immobile boundary condition and discuss the characteristics of this model. However, in the presence of mobile surface-active molecules or processes associated with chemical reactions, material transport or temperature gradients, a surface tension gradient can occur that can balance the tangential shear stress.[82] In the context of dynamic surface force measurements involving bubbles and a solid surface at low concentrations of aqueous electrolyte, such a model has been developed to model the case in which low concentrations of insoluble surfactants are present at the surface of the bubbles.[45,46]

As the shear stress is involved in the boundary condition between two Newtonian fluids, an additional parameter, the viscosity ratio of the dispersed phase to the continuous phase, enters in the formulation of the problem (Fig. 21b). In contrast, for the tangentially immobile boundary condition (Fig. 21c), the viscosity of the dispersed phase does not enter as the velocity of the continuous phase at the boundaries is specified.

The special case of two clean ideal bubbles assumed to have zero internal viscosity that cannot sustain tangential stress at the interface requires a different approach. The vanishing of the tangential stress at such bubble surfaces means that the solution of the lubrication equation (eqn (27)) is a constant. That is, one has plug flow in the lubrication approximation (Fig. 21d). Chesters and Hofman[75] formulated a model for the case of two interacting deformable bubbles in which the non-linear inertia term of the Navier–Stokes equations are retained but the equations are still solved within the lubrication approximation. This model will be considered in Section 6.4 as its behaviour has very different characteristic time scales compared to other models.

6.2 Surfaces with Navier slip

For completeness, we give the film drainage equation between two solid surfaces that obey the Navier slip boundary condition. At a flat surface with an outward normal in the $\pm z$-direction this boundary condition is: $u = \pm\, b\ (\mathrm{d}u/\mathrm{d}z)$ where u is the tangential fluid velocity and b is the slip length (Fig. 21a). In almost all applications, the value of b is not known *a priori*, but is used as a free parameter to fit experimental data.

Thus for the solution of eqn (27) with the possibility of different slip lengths b_o at $z = 0$ and b_h at $z = h$, the drainage equation which replaces the Stokes–Reynolds equation (eqn (30)) has the form

$$\frac{\partial h}{\partial t} = \frac{1}{12\mu r}\frac{\partial}{\partial r}\left(rh^3\frac{\partial p}{\partial r}\right) + \frac{1}{4\mu r}\frac{\partial}{\partial r}\left(r\left[\frac{(b_\mathrm{o}+b_\mathrm{h})h^3 + 4b_\mathrm{o}b_\mathrm{h}h^2}{h + b_\mathrm{o} + b_\mathrm{h}}\right]\frac{\partial p}{\partial r}\right) \tag{36}$$

The schematic velocity profile that corresponds to this drainage equation is illustrated in Fig. 21a.

There are two interesting limiting cases of this result. The condition at a classical "no-slip" can be obtained by setting the slip lengths to zero. If only one surface, say the surface at $z = h$, is that of an ideal bubble—with zero viscosity and cannot sustain tangential stress, we can take the $b_\mathrm{h} \to \infty$. However, as discussed in Section 6.1, we cannot obtain the result for film drainage between the surfaces of two ideal bubbles from eqn (36).

6.3 Two drops with mobile interfaces

When modelling lubrication drainage of the film between two identical drops with internal viscosity μ_d, with interfaces that cannot sustain tangential stress, the solution of eqn (27) will involve the velocity $U(r,t)$ of the interface. The continuity of the tangential stress then gives the following set of coupled integro-differential equations to replace eqn (30):[11,13,112]

$$\frac{\partial h}{\partial t} = \frac{1}{12\mu r}\frac{\partial}{\partial r}\left(rh^3\frac{\partial p}{\partial r}\right) - \frac{1}{r}\frac{\partial}{\partial r}(rhU) \quad \text{(mobile drops)} \tag{37}$$

$$U(r,t) = -\frac{1}{2\mu_d}\int_0^\infty \phi(r,\rho)h(\rho,t)\frac{\partial p(\rho,t)}{\partial \rho}\mathrm{d}\rho \tag{38}$$

$$\phi(r,\rho) = \frac{\rho}{2\pi}\int_0^{\pi} \frac{\cos\ \theta}{\sqrt{r^2+\rho^2-2r\rho\cos\ \theta}}\mathrm{d}\theta \qquad (39)$$

The characteristic behaviour of this model depends on the dimensionless ratio: $m \equiv (\mu/\mu_d)(R/h)^{1/2}$ where R is the characteristic radius of the drops.[13,112] For $m \ll 1$, the interfaces become essentially immobile, while for $m \gg 1$, the drainage rates are much faster and the forces are much smaller than the case for immobile interfaces.[113]

As might be expected, the task of obtaining numerical solutions of eqn (37), (38), (39) and (16) for two such interacting and deformable drops is more difficult than that for immobile interfaces. While there are other formulations for the drainage between drops with mobile interfaces that appear simpler, their treatment of the internal flow is not correct.[114,115] Moreover, there are at present no detailed experimental data where the model of eqn 37, (38) and (39) provides a good quantitative description.

6.4 Chesters–Hofman: two bubbles with mobile interfaces

The interaction between two bubbles in a liquid is a very important and fundamental problem. If the bubbles have fully mobile surfaces that cannot sustain shear stress, the solution to eqn (27) that is valid for low Reynolds numbers would be a constant plug flow velocity that provides no information on the pressure distribution.

Chesters and Hofman[75] considered the interaction between two deformable bubbles with mobile surfaces at high Reynolds numbers. They retained the Reynolds lubrication treatment but regarded the liquid as an inviscid fluid so that only inertial effects are included. In their model, eqn (27) was replaced by the non-linear Navier–Stokes equation for the plug flow velocity $U(r,t)$ in the radial direction in the film:

$$\frac{\partial U}{\partial t} + U\frac{\partial U}{\partial r} = -\frac{1}{\rho}\frac{\partial p}{\partial r} \qquad (40)$$

and the continuity equation can be written as

$$\frac{\partial h}{\partial t} = -\frac{1}{r}\frac{\partial}{\partial r}(rhU) \qquad (41)$$

These equations were solved numerically with the Young–Laplace equation (eqn (16)) to characterise deformations but without the inclusion of a disjoining pressure ($\Pi = 0$). The initial film profile was taken to be $h(r,0) = h_o + r^2/R_o$ that corresponds to spherical bubbles of radius R_o at an initial distance of closest approach h_o. The initial velocity is $U(r,0) = Vr/[2h(r,0)]$ where V is the assumed constant approach velocity of the two bubbles.

Based on the calculations of Chesters and Hofman,[75] we can estimate how long it would take for two bubbles of radius 1.0 mm approaching each other at 10 cm s^{-1} to coalesce. These velocity and size range are typical for bubbles in many industrial applications. Assuming the bubble-in-water surface tension to be 72 mN m^{-1}, a dimple would appear at a separation of 1.4 μm with a film radius of 0.19 mm. The coalescence time would only be about 1.4 ms, counting from the moment the drops would have touched if they did not deform. This is an extremely short time that is at variance with experimental observations. Although the Chesters–Hofman model is often cited in the context of bubble coalescence, experimental verification of this model does not seem to exist. If the model is correct, it might be extremely difficult to observe such small coalescence times.

It should be noted that the Chesters–Hofman model predicts film rupture at the rim, without the need of any Van der Waals attraction or other surface forces. In the model from Sections 3 and 6.3, film rupture would not occur in the absence of attractive surface forces.[116] Instead the film would drain at a decreasing rate without reaching zero thickness. Another peculiarity of this model is that in the case of non-deforming bubbles, eqn (40) and (41) will predict an infinite force between the bubbles. This is due to the slow decay of the pressure field in the radial direction that is inherent in the two-dimensional lubrication formulation of the model.[81] The numerical results of the Chesters–Hofman calculation pertained to deformable bubbles but it is not clear that the divergence problem associated with the slow decay of the pressure field is avoided by surface deformability.

In practice, rising bubbles in water are only observed to exhibit properties consistent with a zero shear stress condition, when extreme care has been taken to de-ionise and clean the water.[60,88,117–119] At low Reynolds numbers, which restrict bubbles with radii with values below 60 μm, the terminal rise velocities of such bubbles in ultra clean water follow the Hadamard–Rybczynski formula that corresponds to a zero shear stress bubble surface.[88] Yet when the same bubbles rise towards a solid titania plate, their rate of approach suggested that the boundary condition at the bubble surface is again a tangentially immobile condition.[62,63] The precise physical reason for this behaviour has yet to be established although trace impurities that originate from the titania plate or accumulate during bubble rise may be implicated.

For the drainage experiments summarised in Sections 4 and 5, there were sufficient trace surface-active impurities in the system to render the bubbles to exhibit tangentially immobile surfaces even though extreme care was taken to avoid such impurities. In actual industrial applications such impurities are in most cases present in abundance.

6.5 Stefan–Reynolds parallel film model

In Sections 6.1–6.4, we have summarised various models that describe interactions involving deformable drops and bubbles and the related film drainage problem. The common feature of all such models is that film drainage with different assumptions about hydrodynamic flow and boundary conditions is coupled with a consistent treatment of interfacial deformations using the Young–Laplace model. However, the resulting system of coupled partial differential equations, even for simple axisymmetric flow, can only be solved numerically. Although perturbation solutions in the limit of weak interactions do give some physical insight into the drainage and coalescence phenomena,[83,84,112] it is only recently that full numerical solutions together with appropriately formulated boundary conditions have been developed to enable quantitative comparison with results obtained from different experimental methods (see Section 3).

The apparent complexity of the Stokes–Reynolds–Young–Laplace model has prompted the development of a number of approximate theories aimed at describing film drainage

dynamics. However, when tested against experimental data, almost all such theories failed to give quantitative agreement.[30]

The most enduring of such approximate solutions of the Stokes–Reynolds–Young–Laplace equations is based on the Stefan–Reynolds Flat Film Model.[19,20] Conceptually it is perhaps also the most confusing because in spite of the inherent inconsistencies of the original basic Stefan–Reynolds model that we shall detail below, numerous extensions and modifications have been proposed to add new features to the model. The physical contents of these modifications are not always well justified[1] and even with the increased complexity, such extensions are not capable of producing the results obtained from the full numerical solution of the original Stokes–Reynolds–Young–Laplace equations given in Sections 4 and 5.

To illustrate the status of the Stefan–Reynolds Flat Film Model and its variants, consider the simple case of a drop (or bubble) approaching a flat solid surface in a continuous phase. Instead of solving the Young–Laplace equation, the deformation is assumed to have the shape of a circular flat disk of some radius, a, oriented parallel to the solid substrate (see Fig. 22). The dimension of the disk radius, a, is not known *a priori*.

As the drop approaches the flat surface under the action of an external force, F_{ext} which in general can be time dependent, the axisymmetric flow of displaced fluid with radial velocity, $u(r,z,t)$, in the film of uniform thickness, $h(t)$, is assumed to be described by low Reynolds number Stokes flow. At the solid surface located at $z = 0$, the familiar boundary condition $u(r,0,t) = 0$ is imposed. If the flat surface of the drop at $z = h$ is tangentially immobile, one then applies the condition $u(r,h,t) = 0$. If on the other hand, the flat surface of the drop is fully mobile such that the shear stress vanishes, the condition $\partial u(r,z,t)/\partial z = 0$ is imposed at $z = h$.

Solving the Stokes flow equations (eqn (27) and (28)) with the above boundary conditions gives the pressure profile due to viscous flow in the film:

$$p(r,t) = p_o - \frac{3\mu}{\beta h^3}\left(\frac{dh}{dt}\right)\left(a^2 - r^2\right), \quad 0 < r < a \tag{42}$$

where p_o is the (constant) pressure in the continuous phase in $r > a$, μ is its viscosity with $\beta = 1$ if the flat surface of the drop is tangentially immobile and $\beta = 4$ if the flat surface of the drop is fully mobile and has zero shear stress.

The result for the quadratic pressure profile in eqn (42) which has a maximum value at $r = 0$ for an approaching drop with $dh/dt < 0$ and decreasing to p_o at $r = a$, presents an immediate inconsistency. In this model, the deformed interface of the drop is assumed to be a flat disk (with zero curvature) at the outset, so according to the Young–Laplace equation, the pressure on either side of such a flat interface must be equal. However, the pressure inside the drop is uniform which is inconsistent with a quadratic pressure distribution given by eqn (42) within the film.

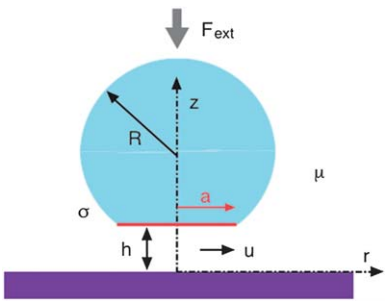

Fig. 22 Schematic of the Stefan–Reynolds Flat Film Model for a drop or bubble with interfacial tension, σ, approaching a flat solid surface.

If there is a disjoining pressure, $\Pi(h)$, due to surface forces acting across the film of area πa^2, the film thinning dynamics is found by a quasi-static force balance in the z direction:

$$-F_{ext}\hat{z} + F_{hydro}\hat{z} + (\pi a^2)\Pi(h)\hat{z} = 0 \tag{43}$$

where the hydrodynamic force is determined from eqn (42) to be

$$F_{hydro} = 2\pi\int_0^a (p - p_o) r dr = -\frac{3\pi\mu a^4}{2\beta h^3}\left(\frac{dh}{dt}\right) \tag{44}$$

and the external force F_{ext} is taken to be positive if it acts to push the drop onto the flat surface.

If the disjoining pressure $\Pi(h)$ has the non-retarded Van der Waals form: $\Pi(h) = -A/(6\pi h^3)$, where A is the Hamaker constant, then eqn (43) and (44) give

$$F_{ext} + \frac{3\pi\mu a^4}{2\beta h^3}\left(\frac{dh}{dt}\right) + (\pi a^2)\frac{A}{6\pi h^3} = 0 \tag{45}$$

Provided the external force F_{ext} and the film radius a are independent of time, eqn (45) can then be integrated[120] to give for $t \geq 0$:

$$t = \frac{\tau}{6\alpha^2}\left\{\log\left[\left(\frac{1+\alpha}{H+\alpha}\right)^3\left(\frac{H^3+\alpha^3}{1+\alpha^3}\right)\right] + \sqrt{12}\left[\arctan\left(\frac{2-\alpha}{\sqrt{3}\alpha}\right) - \arctan\left(\frac{2H-\alpha}{\sqrt{3}\alpha}\right)\right]\right\} \tag{46}$$

where $H(t) \equiv h(t)/h_o$ is the film thickness scaled by the initial thickness, $h_o \equiv h(0)$ with

$$\alpha \equiv \left(\frac{a^2 A}{6h_o^3 F_{ext}}\right)^{1/3} \quad \text{and} \quad \tau \equiv \left(\frac{3\pi\mu a^4}{2\beta h_o^2 F_{ext}}\right). \tag{47}$$

If the Van der Waals interaction is attractive, that is $A > 0$ and $\alpha > 0$, then the coalescence time can be found by setting $H = 0$ in eqn (46). If the Van der Waals interaction is repulsive, that is $A < 0$ and $\alpha < 0$, the film will thin down or thicken (depending on the initial thickness) to the final equilibrium thickness:

$$h_{eq} \equiv h(\infty) = -\left(\frac{a^2 A}{6F_{ext}}\right)^{1/3} \tag{48}$$

For the special case with $A = 0$ (no disjoining pressure), eqn (45) gives the well-known film thinning result:[18]

$$h(t) = h_o\left(1 + \frac{2t}{\tau}\right)^{-1/2} \tag{49}$$

Although the Stefan–Reynolds model appears attractive in being able to furnish analytical results as those illustrated above, in reality its utility is rather limited. From the above derivations, we see that analytic results are only available in the special case where the external force F_{ext} is a known constant, which is suitable for interaction under buoyancy forces, for example. However, the film radius is not known *a priori* which limits the

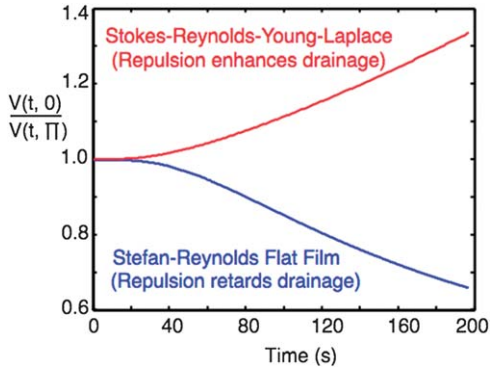

Fig. 23 Comparison of the variation of film volume ratio in the absence and presence of a repulsive disjoining pressure Π according to the Stokes–Reynolds–Young–Laplace model and the Stefan–Reynolds Flat Film Model.[52]

predictive capabilities of the model. There are further developments of the Stefan–Reynolds model in which the film radius a is some assumed function of time[7] but then the analysis of such models generally cannot progress beyond eqn (45) as the integration cannot be carried out analytically. Nonetheless, such theories continue to employ results that were derived under the assumption that the film radius a is a constant, which is not a logically consistent approach.

There are also other extensions of the basic Stefan–Reynolds model that attempt to correct the flat film geometry by adding corrections written in terms of an infinite series of Bessel functions involving unknown coefficients.[89] But despite such mathematical sophistication, these extensions are unable to produce the quantitative agreements with experiments that we have seen in Sections 4 and 5. In fact, all available comparisons[7,23,25,28] between various extensions of the Stefan–Reynolds model are all based on an "average" film thickness that is not well defined in terms of experimentally accessible quantities.

Furthermore with the addition of a repulsive disjoining pressure, the Stefan–Reynolds model predicts the film will drain slower whereas the Stokes–Reynolds–Young–Laplace model predicts a faster drainage rate (Fig. 23) because the additional repulsion increases the thickness of the film at the barrier rim and facilitates faster drainage—which is exactly what is observed in experiments.[2,52]

In summary, the rather restrictive assumptions inherent in the Stefan–Reynolds Flat Film Model and its later variants render its status to a historical curiosity rather than a viable quantitative and predictive theory for the future.

7. Challenges for the future

This review has concentrated on film drainage and coalescence in systems that are relatively pure in composition and symmetrical in the interaction geometry. We examined results in water and in simple alkanes with the possible addition of simple inorganic salts and charged surfactants. The interaction geometries are chosen to have axial symmetry to facilitate comparison with tractable theoretical models. Having examined many experimental results on dynamic deformations and forces obtained using different techniques, we have obtained a good understanding of the fundamental physical principles that operate and have a theoretical framework with accurate predictive capabilities. However, there remain important practical areas where there are rich opportunities for accurate quantitative experiments and theoretical modelling.

One example is the spontaneous loss of axial symmetry in film drainage. In Fig. 24 we show a time sequence of fringes from the drainage of a film of glycerol (70%)–water (30%) mixture (viscosity 23 mPa s) trapped between two approaching silicone oil (47V50) drops (viscosity 50 mPa s, interfacial tension 30 mN m^{-1}).[121] The drops were driven together at 13.3 μm s^{-1} and were then stopped. A dimple in the film had already formed 33 s before the first image, which was taken 80 s after the drops were stopped. A movie file of this symmetry breaking drainage process is available as ESI†.

Examples of an initially axisymmetric film developing asymmetric patterns have been seen elsewhere.[122,130] Burrill and Woods[3] refer to this as even and uneven drainage and noted such occurrences are dependent on the concentration of adsorbed surfactant. It is possible that in this instance, spatial variations in the interfacial tension associated with fluctuations in local concentrations in the glycerol–water mixture may play a role. But a general understanding of the mechanism that triggers asymmetric drainage would be useful.

Chesters observation:[123] '*the entire area of variable interfacial tension is virtually unexplored*' appears to be true today. It is well known that variations in the interfacial tension along the surface can give rise to an interesting phenomenon known generically as the Marangoni effect. Such an effect can also be caused by temperature or solute concentration differences or by mass transfer between phases that create surface tension gradients. Furthermore, mass transfer of a solute could either enhance or delay film drainage by driving interfacial flow and fluid circulation.[124,130]

In Fig. 25 and in a movie in the ESI†, we see an example of Marangoni flow arising from mass transfer of acetone from the dispersed phase (glycerol drops plus 5% acetone) towards the continuous phase (silicone oil 47V50).[125] Effects such as circulatory flow into and out of the film of the continuous phase between the drops are evident. In addition flow vortices are also evident in the interior of the drops. Quantitative experimental

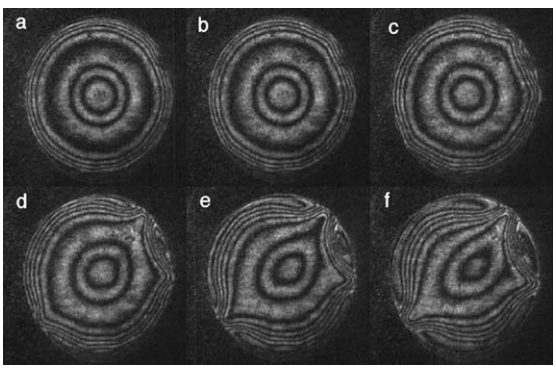

Fig. 24 Fringe patterns of film drainage instability of a glycerol–water mixture between silicone oil drops (radii 1.5 mm). The time interval between successive images (a)–(f) is 16 s. The film thickness at the centre is about 1.5 μm and around 1 μm at the edge. The film has a radius of around 500 μm, the rim is located at the dark broad fringe in the first frame. See text for other details. A movie file is available as ESI†.

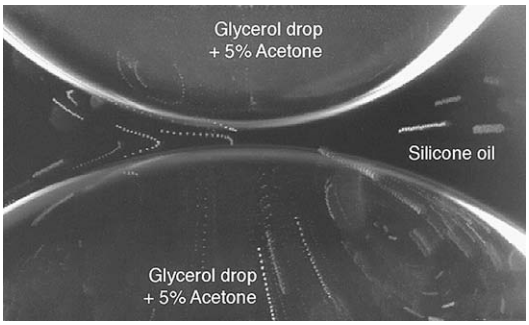

Fig. 25 Marangoni flow due to mass transfer of acetone from two stationary drops of glycerol drops plus 5% acetone into the continuous phase (silicone oil 47V50). The image is a superposition of successive images taken at 1 s apart to visualise the motion of tracer particles. A movie file is available as ESI†.

characterisation of such phenomena is still in its infancy and a fundamental understanding of the general physics that drive such flows is lacking.

So far we have only focussed on experiments where fluid motion is slow enough to be in the low Reynolds number Stokes flow regime. However, many interesting phenomena involving deformable drops and bubbles lie well outside this domain. For instance, the terminal velocity of rising bubbles in the mm size ranges corresponds to Reynolds number of order 500 and inertial effects are therefore important. Many important industrial processes, such as mineral flotation operate with bubbles in this range. When such bubbles collide with solid bodies they can rebound. Detailed experimental studies of such encounters are beginning to emerge[59,60] and theoretical models are still being developed.[126] There are certainly opportunities for more fundamental work in this area.

Another aspect about the coalescence process that we have not explored is the detailed dynamics of how two distinct drops combine to become one. Compared to the time taken for drop approach and film drainage, the formation of a liquid bridge between the drops and its subsequent expansion as the two drops combine occurs over a very short time interval. Experimental investigations require high-speed video observations to record events occurring in a small volume between the drops. This can be partially overcome by using exotic dispersions that comprise mixtures of polymers and colloids[131,132] with ultra low interfacial tensions ($\sim$0.1 μN m^{-1}). From a theoretical modelling viewpoint, parametric studies of such experiments invariably assume tangentially mobile interfaces.[133,134] In the light of many experiments we have reviewed here, consideration should be given to examine the effect of the tangentially immobile boundary condition.

The challenge remains to develop experimental methods underpinned by quantitative theory to improve our understanding in fundamental problems in the interaction involving soft deformable systems.

8. Conclusions

This review has surveyed a broad range of experimental studies on the interaction and coalescence of deformable drops and bubbles in which detailed quantitative spatial and temporal evolution of interfacial deformations or the dynamic forces have been reported. Such results are compared to a quantitative theory that has no adjustable parameters. For systems involving simple liquids with uniform interfacial properties, the combination of hydrodynamic (Stokes) flow and interfacial deformation as described by the Young–Laplace equation—when treated in a self-consistent manner—provides all the physical ingredients that underpin and explain the observed behaviour. Equally, failure to treat the dynamic and the deformation behaviour in a balanced manner simply leads to unnecessary complexities and inconsistencies.

Generalising these observations to other soft or deformable materials, it is clear that quantitative knowledge of the "equation of state", the analogue of the Young–Laplace equation, that relates deformations and applied forces or stresses on the soft material is key to a quantitative understanding of the dynamics of soft materials. This should be taken into consideration when developing new experimental tools and protocols when the objective is to make quantitative studies of dynamic interactions involving soft matter.

Appendix A: outer drop shape

In this Appendix, we derive the outer solution of the Young–Laplace equation for the shape of a sessile drop with constant interfacial tension, σ, that has an external force, $F(t)$, acting on its apex within a small interaction zone of dimension: $r \approx a$, with a small compared to the drop size. Where a dimple exists, the dimple radius r_{rim} would be of order a. The outer solution is valid for $r > a$. The inner asymptotic form of this outer solution in the limit $r \rightarrow a$ will be matched to the inner solution of the film profile found in Section 3.1.3. The idea is that we only need to solve (numerically) the Stokes–Reynolds–Young–Laplace equations for the evolution of the film thickness between interacting drops within the interaction zone. The outer solution will furnish the appropriate boundary condition at the outer edge of the film. This approach allows us to obtain accurate numerical solutions of the shape of the drop in the interaction zone without integrating over the entire drop.

When the dimension of the interaction zone is small compared to the drop size, a condition that is well satisfied in the experiments we discussed, we can obtain an analytic form of the outer solution. Here we use the approach of Chesters[127] that provided a simple and physically perspicuous derivation. Earlier attempts at the same problem[68,79] were based on a Cartesian coordinate system that was more complex and led to various algebraic errors that were subsequently remedied by Bardos.[128]

The key results of this Appendix are in eqn (A14) and (A16).

We also give an analysis of the effects of bubble compressibility on deformations to show that for bubbles in water, compressibility will be important for small bubbles with radii below about 1 μm.

We start with the first integral of the Young–Laplace equation expressed in terms of the tangent angle φ (Fig. 2) given in eqn (8). We recall that this result is valid outside the interaction zone. To simplify the notation, we define $G(t) \equiv F(t)/(2\pi\sigma)$, a quantity with the dimension of length that is expressed in terms of the force acting on the drop, $F(t)$, see eqn (7) and denote the Laplace radius, R_{L} by $R \equiv R_{\mathrm{L}}$. Thus eqn (8) becomes

$$r\sin\ \varphi = \frac{r^2}{R} - G(t), \quad \text{for } r \gg a \tag{A1}$$

This can be solved for r to give

$$r = \frac{1}{2}R\left(\sin\varphi + \sqrt{\sin^2\varphi + 4G/R}\right) \tag{A2}$$

As we approach the apex of the drop from outside the interaction zone by taking the limit $r \to a$ and $\varphi \to 0$, we see from eqn (A2) that $r \to [GR]^{1/2} \equiv [FR/(2\pi\sigma)]^{1/2}$. Thus the length $(GR)^{1/2}$ is a natural measure of the extent of the interaction zone.

Using eqn (A2), we integrate the identity: $\mathrm{d}z/\mathrm{d}r = -\tan\ \varphi$ (Fig. 2) to obtain the height, $z(r)$, of the drop outside the interaction zone:

$$z(r) = \int_{\theta}^{\varphi} \frac{\mathrm{d}z}{\mathrm{d}r}\frac{\mathrm{d}r}{\mathrm{d}\varphi}\mathrm{d}\varphi = -\frac{1}{2}R\int_{\theta}^{\varphi} \sin\ \varphi\left(1 + \frac{\sin\ \varphi}{\sqrt{\sin^2\ \varphi + 4G/R}}\right)\mathrm{d}\varphi \tag{A3}$$

This result can be expressed in terms of elliptic integrals. However, we are only interested in the result for $z(r)$ at small forces as characterised by the limit $(G/R) = F/(2\pi\sigma R) \ll 1$. In this case, deviations of the contact angle: $\theta = \theta_o + \delta\theta$ and the Laplace radius $R = R_o + \delta R$ due to interactions from the unperturbed values, θ_o and R_o, are small.

For ease of matching with the inner solutions in Section 3.1.3 we only expand the lower limit of integration, θ, and the integrand in eqn (A3) to linear order in $\delta\theta$, δR and G to give

$$\begin{aligned} z(r) &= -R\int_{\theta_o}^{\varphi} \sin\ \varphi\mathrm{d}\varphi + \{R_o\sin\ \theta_o\}\delta\theta + \left\{\int_{\theta_o}^{\varphi}\frac{1}{\sin\ \varphi}\mathrm{d}\varphi\right\}G \\ &= R\cos\ \varphi|_{\theta_o}^{\varphi} + \{R_o\sin\ \theta_o\}\delta\theta - \left\{\frac{1}{2}\log\left(\frac{1+\cos\ \varphi}{1-\cos\ \varphi}\right)\Big|_{\theta_o}^{\varphi}\right\}G \end{aligned} \tag{A4}$$

The form of $z(r)$ near the apex of the drop corresponds to the limit $\varphi \to 0$, where from eqn (A1) we have

$$\sin\ \varphi \approx \varphi + \ldots = \frac{r}{R} - \frac{G}{r} \tag{A5}$$

$$\cos\ \varphi \approx 1 - \frac{1}{2}\varphi^2 + \ldots = 1 - \frac{r^2}{2R^2} + \frac{G}{R} + O(G^2) \tag{A6}$$

and inserting these into eqn (A4) for $z(r)$ gives as $r \to a$

$$\begin{aligned} z(r) \to R_o(1-\cos\ \theta_o) - \frac{r^2}{2R} + \{1-\cos\ \theta_o\}\delta R + \{R_o\sin\ \theta_o\}\delta\theta \\ + \left\{\log\left(\frac{r}{2R_o}\right) + 1 + \frac{1}{2}\log\left(\frac{1+\cos\ \theta_o}{1-\cos\ \theta_o}\right)\right\}G \end{aligned} \tag{A7}$$

This is the limiting form of the outer solution that we seek on approaching the interaction zone ($\varphi \to 0$) from outside the film, $r \to a$ from above. This result is correct to linear order in $\delta\theta$, δR and G. The first term: $R_o(1 - \cos\ \theta_o)$, is just the height of the undeformed drop. The quadratic term in r is scaled by the Laplace radius, R, while the remaining constants represent changes to the drop height due to the external force.

The remaining task is to relate the perturbation, $\delta\theta$ and δR, to the total force, $F = 2\pi\sigma G$, acting on the drop. We assume the drop/bubble maintains constant volume as it deforms. The effects of a compressible bubble will be considered later.

The volume of the drop, V_d, can be found by integrating the outer solution:

$$\begin{aligned} V_d &= \int_0^{z(0)} \pi r^2\mathrm{d}z = \int_{\theta}^{0} \pi r^2\frac{\mathrm{d}z}{\mathrm{d}r}\frac{\mathrm{d}r}{d\varphi}d\varphi \\ &= \frac{\pi R^3}{8}\int_0^{\theta}\frac{\left(\sin\ \varphi + \sqrt{\sin^2\ \varphi + 4G/R}\right)^3}{\sqrt{\sin^2\ \varphi + 4G/R}}\sin\varphi\,\mathrm{d}\varphi \end{aligned} \tag{A8}$$

The constant volume constraint can be expressed as

$$\begin{aligned} \delta V_d &= \left(\frac{\partial V_d}{\partial\theta}\right)_o\delta\theta + \left(\frac{\partial V_d}{\partial R}\right)_o\delta R + \left(\frac{\partial V_d}{\partial G}\right)_o G = 0 \\ &= \{\pi R_o^3\sin^3\ \theta_o\}\delta\theta \\ &\quad + \left\{\pi R_o^2(1-\cos\ \theta_o)^2(2+\cos\ \theta_o)\right\}\delta R \\ &\quad + \{\pi R_o^2(1-\cos\ \theta_o)\}G = 0 \end{aligned} \tag{A9}$$

which gives one relation between $\delta\theta$, δR and G.

A second relation between $\delta\theta$, δR and G can be found by specifying how the drop responds to the external force. We will consider two simple possibilities: (1) the drop can deform by maintaining the three phase contact position pinned at r_1 (see Fig. 2), so that the contact angle changes or (2) by maintaining a constant contact angle θ_o while the position of the three phase contact line is free to move along the substrate.

A.1 Pinned contact line at r_1: $\delta r_1 = 0$

At the pinned contact line: $r_1 = R_o\sin\ \theta_o$ and $\varphi = \theta = \theta_o + \delta\theta$, eqn (A1) becomes

$$r_1^2 - r_1 R\sin\ (\theta_o + \delta\theta) - RG = 0 \tag{A10}$$

By expanding this to linear order in $\delta\theta$, $\delta R = R - R_o$ and G we obtain the second relation between $\delta\theta$, δR and G

$$\{\sin^2\ \theta_o\}\delta R + \{R_o\ \sin\ \theta_o\cos\ \theta_o\}\delta\theta + G = 0 \tag{A11}$$

Now we can obtain the desired relation between δR and G by eliminating $\delta\theta$ between eqn (A9) and (A11)

$$\delta R = \frac{-1}{(1-\cos\ \theta_o)}G \tag{A12}$$

Similarly, by eliminating δR between eqn (A9) and (A11) we obtain $\delta\theta$ in terms of G

$$\delta\theta = \frac{1}{R_o\sin\ \theta_o}G \tag{A13}$$

Finally, using eqn (A12) and (A13) in (A7) we have

$$z(r) = R_o(1-\cos\ \theta_o) - \frac{r^2}{2R_L} + \frac{F(t)}{2\pi\sigma}\left\{\log\left(\frac{r}{2R_o}\right) + 1 + \frac{1}{2}\log\left(\frac{1+\cos\ \theta_o}{1-\cos\ \theta_o}\right)\right\} \quad \text{(A14)}$$

which is the limiting form of the outer solution we are seeking as one approaches the interaction zone ($\varphi \rightarrow 0$) for a drop deforming under the pinned contact line condition. We have restored the notation for the Laplace radius: $R \equiv R_L$ to conform to the notation as in the main text.

A.2 Constant contact angle θ_o: $\delta\theta = 0$

For deformations at constant contact angle, θ_o, we can immediately set $\delta\theta = 0$ in eqn (A9) to find the corresponding relation between δR and G

$$\delta R = \frac{-1}{(1-\cos\ \theta_o)(2+\cos\ \theta_o)} G \quad \text{(A15)}$$

And by inserting this into eqn (A7) with $\delta\theta = 0$, we have the limiting form of the required outer solution as one approaches the interaction zone ($\varphi \rightarrow 0$) for deformation under the constant contact angle condition (after restoring the notation for the Laplace radius $R \equiv R_L$ as in the main text)

$$z(r) = R_o(1-\cos\ \theta_o) - \frac{r^2}{2R_L} + \frac{F(t)}{2\pi\sigma}\left\{\log\left(\frac{r}{2R_o}\right) + 1 + \frac{1}{2}\log\left(\frac{1+\cos\ \theta_o}{1-\cos\ \theta_o}\right) - \frac{1}{2+\cos\ \theta_o}\right\} \quad \text{(A16)}$$

All the above results are identical to those obtained by Bardos,[128] but the derivation given here is more compact and physically transparent without the need to treat the cases of acute and obtuse contact angles separately.

A.3 Bubble compressibility

We can estimate the effects of bubble compressibility by assuming that the internal pressure, P_{in}, of the bubble containing N molecules of ideal gas and its volume V_b obeys: $P_{in}V_b = NkT$, where k is the Boltzmann constant. Using the Young–Laplace equation: $P_{in} = P_{out} + 2\sigma/R$, where $P_{out} \approx 1$ atm, the bubble volume can be expressed as:

$$V_b(R) = \frac{NkT}{(P_{out} + 2\sigma/R)} \quad \text{(A17)}$$

Thus the variation of the bubble volume with a change in the Laplace radius $R = R_o + \delta R$ is

$$\delta V_b = \left(\frac{\partial V_b}{\partial R}\right)_o \delta R = \left\{\frac{V_b(R_o)}{R_o}\frac{2\sigma/R_o}{P_{out} + 2\sigma/R_o}\right\}\delta R \quad \text{(A18)}$$

If we assume terms involving $\cos\ \theta_o$ in eqn (A9) are of order unity, the magnitude of the coefficient of δR in eqn (A9) will be comparable to that of the coefficient of δR in eqn (A18) when $(2\sigma/R_o) \approx P_{out} \approx 1$ atm. In other words, for a bubble in water, bubble compressibility is important for bubbles with radii below about 1 μm. For a bubble radius of 70 μm, bubble compressibility contributes about a 1% effect.

Appendix B: results from scaled equations

Due to the very different characteristic dimensions of the film thickness, film radius and drop size, appropriate scaling of the governing equations is essential for developing robust numerical solutions. General features of the problem can be extracted by working with dimensionless or even double dimensionless forms.[123] Here we will consider the drainage of the film between two identical drops when they approach either at constant velocity (so that the force between the drops will vary) or at constant force (so the relative velocity will vary).

B.1 Two identical drops driven at constant velocity

This case corresponds to experiments when the drops are anchored on solid substrates or have emerged and then pinned at the orifice of capillary tubes with undeformed radius, R_o. The substrates or the capillary tubes are driven at constant velocity, V, to cause the drops to approach or separate. A key parameter of the problem is the capillary number $Ca \equiv \mu V/\sigma$ that measures the ratio of viscous forces to surface tension forces. For the experimental systems considered here, the drive speed is low and we always have $Ca \ll 1$.

The Stokes–Reynolds–Young–Laplace equations can be non-dimensionalised into a universal form with the following scaling parameters[123] for the

film thickness: h, $z \approx Ca^{1/2}R_o$,
radial coordinate: $r \approx Ca^{1/4}R_o$,
time: $t \approx Ca^{1/2}R_o/V$,
pressure: $p \approx \sigma/R_o$ and
force: $F \approx (\sigma/R_o)(Ca^{1/4}R_o)^2 \approx Ca^{1/2}\sigma R_o$.

Denoting scaled variables by asterisks, the Stokes–Reynolds equation that describes film drainage between two drops with immobile boundary conditions at the drop surfaces, eqn (30), becomes

$$\frac{\partial h^*}{\partial t^*} = \frac{1}{12r^*}\frac{\partial}{\partial r^*}\left(r^* h^{*3}\frac{\partial p^*}{\partial r^*}\right) \quad \text{(immobile interfaces)} \quad \text{(A19)}$$

and the Young–Laplace equation (eqn (16)) for two identical drops becomes

$$\frac{1}{2r^*}\frac{\partial}{\partial r^*}\left(r^*\frac{\partial h^*}{\partial r^*}\right) = 2 - \left(\frac{R_o}{\sigma}\right)\Pi - p^* \quad \text{(identical drops)} \quad \text{(A20)}$$

with the initial condition, eqn (31)

$$h^*(r^*,0) = h_o^* + (r^*)^2 \quad \text{(A21)}$$

These equations contain no other physical parameters apart from the scaled disjoining pressure. The boundary condition at r^*_{max}, obtained by differentiating eqn (22) with respect to time, t, and setting $dD(t)/dt = -V$, has a weak logarithmic dependence on the capillary number Ca:

$$\frac{\partial h^*(r^*_{max}, t^*)}{\partial t^*} = -1 - \frac{1}{\pi}\frac{dF^*}{dt^*}\left\{\log\left(\frac{1}{2}Ca^{1/4}r^*_{max}\right) + B(\theta_o)\right\} \quad \text{(A22)}$$

Numerical solutions[44] of these equations in the absence of a disjoining pressure, $\Pi = 0$, revealed that under such constant velocity approach, the initially parabolic film profile will first exhibit a dimple when the central separation reaches the value

$$h(r = 0,t) = cR\mathrm{Ca}^{1/2} \equiv h_{\mathrm{dimple}} \quad \text{(A23)}$$

with c being a constant that ranges from ~0.3 for Ca $\approx 10^{-10}$ to ~0.5 for $Ca \approx 10^{-4}$. Note that in Manica *et al.*[44] and Chan *et al.*[83] the corresponding constant quoted for h_{dimple} was for a drop against a solid plate, namely, ~0.4 for $Ca \approx 10^{-10}$ and ~0.7 for $Ca \approx 10^{-4}$. For two approaching identical drops, the maximum shear stress is about $\tau_{\max} \approx 0.5\mathrm{Ca}^{1/4}\sigma/R_{\mathrm{o}}$ and occurs at the rim position, $r_{\mathrm{rim}} \approx 3\mathrm{Ca}^{1/4}R_{\mathrm{o}}$. The time for the thickness at r_{rim} to drain from h_{dimple} to ½h_{dimple} is about $t \approx 50\mathrm{Ca}^{1/2}R_{\mathrm{o}}/V$. The film thickness at the rim thins slowly, but the radius of the rim, r_{rim}, continues to increase with time.

B.2 Two identical drops driven at constant force

The constant velocity case exhibited a weak dependence of the results on the capillary number, Ca, in the term proportional to $\mathrm{d}F/\mathrm{d}t$ in the boundary condition. The constant force case corresponds to $\mathrm{d}F/\mathrm{d}t = 0$. In the absence of a disjoining pressure, $\Pi = 0$, this 'leads to a universal set of equations containing no parameters at all'[123] that has the same form as eqn (A19) and (A20) using the scaling parameters:

film thickness: h, $z \approx F/\sigma$,
radial coordinate: $r \approx (FR_{\mathrm{o}}/\sigma)^{1/2}$,
time: $t \approx \mu R_{\mathrm{o}}^2/F$ and
pressure: $p \approx \sigma/R_{\mathrm{o}}$

A numerical study of the governing equations shows that the dimple in the film will first appear at the separation

$$h(r = 0,t) = 0.08(F/\sigma) \equiv h_{\mathrm{dimple}} \quad \text{(A24)}$$

Just after the time of dimple formation, the shear stress takes on the maximum value of $\tau_{\max} \approx 0.25(F\sigma/R_{\mathrm{o}}^3)^{1/2}$ around the rim region of the film and subsequently gradually decreases as film drainage progresses. The rim radius approaches a constant value of $r_{\mathrm{rim}} \approx 0.375\ (FR_{\mathrm{o}}/\sigma)^{1/2}$ for times larger than $t \approx 200\ \mu R_{\mathrm{o}}^2/F$. The rim thickness drains from h_{dimple} to ½h_{dimple} in around $t \approx 100\ \mu R_{\mathrm{o}}^2/F$ and to about $0.1h_{\mathrm{dimple}}$ at $t \approx 1000\mu R_{\mathrm{o}}^2/F$, with an asymptotic time dependence[112] of $t^{-2/3}$.

The general results presented here were derived from a scaling of the equations determined by the characteristic constraints of the experimental situation *e.g.* constant velocity or constant force. A recent attempt to model a similar dynamic drainage phenomenon[71] used a scaling analysis appropriate to an unrelated two-dimensional flow problem so quantitative comparisons of the predictions of this theory with experiments were not possible.

Acknowledgements

We have benefited enormously from discussions with and lessons provided by Steven Carnie, Jean-Philippe Chevaillier (who generated the movie files corresponding to Fig. 24 and 25), Lucy Clasohm, Jason Connor, Ray Dagastine, Scott Edwards, Christophe Gourdon, Franz Grieser, Roger Horn, Ofer Manor, Olivier Masbernat, Geoff Stevens, Hemayet Uddin, Ivan Vakarelski and Grant Webber. The experimental results of Fig. 6, 7, 24 and 25 were obtained by E.K. at the Institut de Mécanique des Fluides/Ecole National d'Ingénieurs de Génie Chimique in Toulouse, France. Partial support provided to D.Y.C.C. by the Australian Research Council through the Discovery Projects and Linkage Projects schemes is gratefully acknowledged.

References

1 A. Sanfeld and A. Steinchen, *Adv. Colloid Interface Sci.*, 2008, **140**, 1.
2 L. R. Fisher, D. Hewitt, E. E. Mitchell, J. Ralston and J. Wolfe, *Adv. Colloid Interface Sci.*, 1992, **39**, 397.
3 K. A. Burrill and D. R. Woods, *J. Colloid Interface Sci.*, 1973, **42**, 15.
4 B. Derjaguin and M. Kussakov, *Acta Physicochim. URSS*, 1939, **10**, 25; Reprinted in: *Prog. Surf. Sci.*, 1992, 40, 26.
5 B. Derjaguin and L. Landau, *Acta Physicochim. URSS*, 1941, **14**, 663; Reprinted in: *Prog. Surf. Sci.*, 1993, 43, 30.
6 E. J. W. Verwey and J. Th. G. Overbeek, *Theory of the Stability of Lyophobic Colloids*, Elsevier, Amsterdam, 1948.
7 I. B. Ivanov, D. S. Dimitrov, P. Somasundaran and R. K. Jain, *Chem. Eng. Sci.*, 1985, **40**, 137.
8 C. Y. Lin and J. C. Slattery, *AIChE J.*, 1982, **28**, 147.
9 J. D. Chen and J. C. Slattery, *AIChE J.*, 1982, **28**, 955.
10 J. D. Chen, *J. Colloid Interface Sci.*, 1984, **98**, 329.
11 S. Abid and A. K. Chesters, *Int. J. Multiphase Flow*, 1994, **20**, 613.
12 A. Saboni, C. Gourdon and A. K. Chesters, *J. Colloid Interface Sci.*, 1995, **175**, 27.
13 R. H. Davis, J. A. Schonberg and J. M. Rallison, *Phys. Fluids A*, 1989, **1**, 77.
14 M. A. Rother, A. Z. Zinchenko and R. H. Davis, *J. Fluid Mech.*, 1997, **346**, 117.
15 A. K. Chesters and I. B. Bazhlekov, *J. Colloid Interface Sci.*, 2000, **230**, 229.
16 I. B. Bazhlekov, A. K. Chesters and F. N. van de Vosse, *Int. J. Multiphase Flow*, 2000, **26**, 445.
17 K.-B. Fu and J. C. Slattery, *J. Colloid Interface Sci.*, 2007, **315**, 569.
18 A. Scheludko, *Adv. Colloid Interface Sci.*, 1967, **1**, 391.
19 J. Stefan, *Sitzungsber. Akad. Wiss. Wien, Math.-Naturwiss. Kl., Abt. 2A*, 1874, **69**, 713.
20 O. Reynolds, *Philos. Trans. R. Soc. London, Ser. A*, 1886, **177**, 157.
21 I. B. Ivanov, *Thin Liquid Films: Fundamentals and Applications*, Marcel Dekker Inc., New York, 1988.
22 B. P. Radoev, A. D. Scheludko and E. D. Manev, *J. Colloid Interface Sci.*, 1983, **95**, 254.
23 E. Manev, R. Tsekov and B. Radoev, *J. Dispersion Sci. Technol.*, 1997, **18**, 769.
24 D. S. Valkovska, K. D. Danov and I. B. Ivanov, *Adv. Colloid Interface Sci.*, 2002, **96**, 101.
25 J. E. Coons, P. J. Halley, S. A. McGlashan and T. Tran-Cong, *Adv. Colloid Interface Sci.*, 2003, **105**, 3.
26 R. Tsekov and E. Evstatieva, *Prog. Colloid Polym. Sci.*, 2004, **126**, 93.
27 E. D. Manev and A. V. Nguyen, *Int. J. Miner. Process.*, 2005, **77**, 1.
28 E. D. Manev and A. V. Nguyen, *Adv. Colloid Interface Sci.*, 2005, **114–115**, 133.
29 L. R. Fisher, E. E. Mitchell, D. Hewitt, J. Ralston and J. Wolfe, *Colloids Surf.*, 1991, **52**, 163.
30 D. Hewitt, D. Fornasiero, J. Ralston and L. R. Fisher, *J. Chem. Soc., Faraday Trans.*, 1993, **89**, 817.
31 E. Klaseboer, J. Ph. Chevaillier, C. Gourdon and O. Masbernat, *J. Colloid Interface Sci.*, 2000, **229**, 274.
32 D. E. Aston and J. C. Berg, Quantitative analysis of fluid interface–atomic force microscopy, *J. Colloid Interface Sci.*, 2001, **235**, 162.
33 J. N. Connor and R. G. Horn, *Langmuir*, 2001, **17**, 7194.
34 J. N. Connor and R. G. Horn, *Faraday Discuss.*, 2003, **123**, 193.
35 S. A. Nespolo, D. Y. C. Chan, F. Grieser, P. G. Hartley and G. W. Stevens, *Langmuir*, 2003, **19**, 2124.
36 A. P. Gunning, A. R. Mackie, P. J. Wilde and V. J. Morris, *Langmuir*, 2004, **20**, 116.
37 L. Y. Clasohm, J. N. Connor, O. I. Vinogradova and R. G. Horn, *Langmuir*, 2005, **21**, 8243.
38 R. A. Pushkarova and R. G. Horn, *Colloids Surf., A*, 2005, **261**, 147.
39 R. G. Horn, M. Asadullah and J. N. Connor, *Langmuir*, 2006, **22**, 2610.
40 R. R. Dagastine, R. Manica, S. L. Carnie, D. Y. C. Chan, G. W. Stevens and F. Grieser, *Science*, 2006, **313**, 210.

41 R. Manica, J. N. Connor, S. L. Carnie, R. G. Horn and D. Y. C. Chan, *Langmuir*, 2007, **23**, 626.
42 R. Manica, J. N. Connor, L. Y. Clasohm, S. L. Carnie, R. G. Horn and D. Y. C. Chan, *Langmuir*, 2008, **24**, 1382.
43 R. Manica, J. N. Connor, R. R. Dagastine, S. L. Carnie, R. G. Horn and D. Y. C. Chan, *Phys. Fluids*, 2008, **20**, 032101.
44 R. Manica, E. Klaseboer and D. Y. C. Chan, *Soft Matter*, 2008, **4**, 1613.
45 O. Manor, I. U. Vakarelski, X. Tang, S. J. O'Shea, G. W. Stevens, F. Grieser, R. R. Dagastine and D. Y. C. Chan, *Phys. Rev. Lett.*, 2008, **101**, 024501.
46 O. Manor, I. U. Vakarelski, G. W. Stevens, F. Grieser, R. R. Dagastine and D. Y. C. Chan, *Langmuir*, 2008, **24**, 11533.
47 G. B. Webber, R. Manica, S. A. Edwards, S. L. Carnie, G. W. Stevens, F. Grieser, R. R. Dagastine and D. Y. C. Chan, *J. Phys. Chem. C*, 2008, **112**, 567.
48 V. V. Yaminsky, S. Ohnishi, E. A. Vogler and R. G. Horn, *Langmuir*, 2010, **26**, 8061.
49 V. V. Yaminsky, S. Ohnishi, E. A. Vogler and R. G. Horn, *Langmuir*, 2010, **26**, 8075.
50 R. R. Dagastine, G. B. Webber, R. Manica, G. W. Stevens, F. Grieser and D. Y. C. Chan, *Langmuir*, 2010, **26**, 11921.
51 I. U. Vakarelski, R. Manica, X. Tang, S. J. O'Shea, G. W. Stevens, F. Grieser, R. R. Dagastine and D. Y. C. Chan, *Proc. Natl. Acad. Sci. U. S. A.*, 2010, **107**, 11177.
52 R. Manica and D. Y. C. Chan, *Phys. Chem. Chem. Phys.*, DOI: 10.1039/c0cp00677g.
53 S. P. Frankel and K. J. Mysels, *J. Phys. Chem.*, 1962, **66**, 190.
54 S. Hartland and J. D. Robinson, *J. Colloid Interface Sci.*, 1977, **60**, 72.
55 D. S. Dimitrov and I. B. Ivanov, *J. Colloid interface Sci.*, 1978, **64**, 97.
56 R. K. Jain and I. B. Ivanov, *J. Chem. Soc., Faraday Trans. 2*, 1980, **76**, 250.
57 P. A. Kralchevsky and N. D. Denkov, *Colloids Surf., A*, 2006, **282–283**, 1.
58 M. Borrell and L. G. Leal, *J. Colloid Interface Sci.*, 2008, **319**, 263.
59 H.-K. Tsao and D. L. Koch, *Phys. Fluids*, 1997, **9**, 44.
60 K. Malysa, M. Krasowska and M. Krzan, *Adv. Colloid Interface Sci.*, 2005, **114–115**, 205.
61 M. Krasowska and K. Malysa, *Adv. Colloid Interface Sci.*, 2007, **134–135**, 138.
62 L. Parkinson and J. Ralston, *J. Phys. Chem. C*, 2010, **114**, 2273.
63 R. Manica, L. Parkinson, J. Ralston and D. Y. C. Chan, *J. Phys. Chem. C*, 2010, **114**, 1942.
64 W. A. Ducker, Z. Xu and J. N. Israelachvili, *Langmuir*, 1994, **10**, 3279.
65 H.-J. Butt, *J. Colloid Interface Sci.*, 1994, **166**, 109.
66 H.-J. Butt, R. Berger, E. Bonaccurso, Y. Chen and J. Wang, *Adv. Colloid Interface Sci.*, 2007, **133**, 91.
67 E. K. Yeh, J. Newman and C. J. Radke, *Colloids Surf., A*, 1999, **156**, 525.
68 D. Y. C. Chan, R. R. Dagastine and L. R. White, *J. Colloid Interface Sci.*, 2001, **236**, 141.
69 D. S. Valkovska, K. D. Danov and I. B. Ivanov, *Colloids Surf., A*, 1999, **156**, 547.
70 R. S. Allan, G. E. Charles and S. G. Mason, *J. Colloid Sci.*, 1961, **16**, 150.
71 V. S. Ajaev, R. Tsekov and O. I. Vinogradova, *Phys. Rev. E: Stat., Nonlinear, Soft Matter Phys.*, 2008, **78**, 031602.
72 D. Platikanov, *J. Phys. Chem.*, 1964, **68**, 3619.
73 K. A. Burrill and D. R. Woods, *J. Colloid Interface Sci.*, 1969, **30**, 511.
74 K. A. Burrill and D. R. Woods, *J. Colloid Interface Sci.*, 1973, **42**, 35.
75 K. Chesters and G. Hofman, *Appl. Sci. Res.*, 1982, **38**, 353.
76 S. Hartland, B. Yang and S. A. K. Jeelani, *Chem. Eng. Sci.*, 1994, **49**, 1313.
77 K. D. Danov, T. D. Gurkov, T. Dimitrova, I. B. Ivanov and D. Smith, *J. Colloid Interface Sci.*, 1997, **188**, 313.
78 D. Y. C. Chan, O. Manor, J. N. Connor and R. G. Horn, *Soft Matter*, 2008, **4**, 471.
79 P. Attard and S. J. Miklavcic, *Langmuir*, 2001, **17**, 8217.
80 G. K. Batchelor, *An Introduction to Fluid Dynamics*, Cambridge University Press, 1967.
81 L. G. Leal, *Advanced Transport Phenomena: Fluid Mechanics and Convective Transport*, Cambridge University Press, 2007.
82 V. G. Levich, *Physicochemical Hydrodynamics*, Prentice Hall, 1962, ch. 8.
83 D. Y. C. Chan, E. Klaseboer and R. Manica, *Soft Matter*, 2009, **5**, 2858.
84 D. Y. C. Chan, E. Klaseboer and R. Manica, *Soft Matter*, 2010, **6**, 1809.
85 A. Lai, N. Bremond and H. A. Stone, *J. Fluid Mech.*, 2009, **632**, 97.
86 F. Baldessari and L. G. Leal, *Phys. Fluids*, 2006, **18**, 013602.
87 S. L. Carnie, D. Y. C. Chan, C. Lewis, R. Manica and R. R. Dagastine, *Langmuir*, 2005, **21**, 2912.
88 L. Parkinson, R. Sedev, D. Fornasiero and J. Ralston, *J. Colloid Interface Sci.*, 2008, **322**, 168.
89 R. Tsekov and O. I. Vinogradova, *Langmuir*, 2005, **21**, 12090.
90 V. S. Ajaev, R. Tsekov and O. I. Vinogradova, *Phys. Fluids*, 2007, **19**, 061702.
91 S. Guido and M. Simeone, *J. Fluid Mech.*, 1998, **357**, 1.
92 L. G. Leal, *Phys. Fluids*, 2004, **16**, 1833.
93 Y. Yoon, F. Baldessari, H. C. Ceniceros and L. G. Leal, *Phys. Fluids*, 2007, **19**, 102102.
94 Y. Yoon, M. Borrell, C. C. Park and L. G. Leal, *J. Fluid Mech.*, 2005, **525**, 355.
95 D. Z. Gunes, X. Clain, O. Breton, G. Mayor and A. S. Burbidge, *J. Colloid Interface Sci.*, 2010, **343**, 79.
96 N. Bremond, A. R. Thiam and J. Bibette, *Phys. Rev. Lett.*, 2008, **100**, 024501.
97 J.-L. Joye, C. A. Miller and G. J. Hirasaki, *Langmuir*, 1992, **8**, 3083.
98 G. Singh, C. A. Miller and G. J. Hirasaki, *J. Colloid Interface Sci.*, 1997, **187**, 334.
99 C. Neto, D. R. Evans, E. Bonaccurso, H.-J. Butt and V. S. J. Craig, *Rep. Prog. Phys.*, 2005, **68**, 2859.
100 E. Lauga, M. P. Brenner and H. A. Stone, Microfluidics: the No-Slip Boundary Condition, in *Handbook of Experimental Fluid Dynamics*, ed. C. Tropea, A. Yarin and J. F. Foss, Springer, New York, 2007, ch. 19, pp. 1219–1240.
101 C. L. M. H. Navier, *Mem. Acad. Sci. Inst. Fr.*, 1823, **6**, 389.
102 O. I. Vinogradova, *Langmuir*, 1995, **11**, 2213.
103 O. I. Vinogradova, *Int. J. Miner. Process.*, 1999, **56**, 31.
104 N. Ishida, T. Inoue, M. Miyahara and K. Higashitani, *Langmuir*, 2000, **16**, 6377.
105 D. Y. C. Chan, M. H. Uddin, K. L. Cho, I. I. Law, R. N. Lamb, G. W. Stevens, F. Grieser and R. R. Dagastine, *Faraday Discuss.*, 2009, **143**, 151.
106 V. S. J. Craig, C. Neto and D. R. M. Williams, *Phys. Rev. Lett.*, 2001, **87**, 054504.
107 E. Bonaccurso, M. Kappl and H.-J. Butt, *Phys. Rev. Lett.*, 2002, **88**, 076103.
108 E. Bonaccurso, H.-J. Butt and V. S. J. Craig, *Phys. Rev. Lett.*, 2003, **90**, 144501.
109 C. D. F. Honig and W. A. Ducker, *Phys. Rev. Lett.*, 2007, **98**, 028305.
110 C. D. F. Honig and W. A. Ducker, *J. Phys. Chem. C*, 2008, **112**, 17324.
111 C. L. Henry and V. S. J. Craig, *Phys. Chem. Chem. Phys.*, 2009, **11**, 9514.
112 S. G. Yiantsios and R. H. Davis, *J. Fluid Mech.*, 1990, **217**, 547.
113 S. A. Edwards, S. L. Carnie, O. Manor and D. Y. C. Chan, *Langmuir*, 2009, **25**, 3352.
114 L. Y. Yeo, O. K. Matar, E. S. P. de Ortiz and G. F. Hewitt, *J. Colloid Interface Sci.*, 2001, **241**, 233.
115 L. Y. Yeo, O. K. Matar, E. S. P. de Ortiz and G. F. Hewitt, *J. Colloid Interface Sci.*, 2003, **257**, 93.
116 S. G. Yiantsios and R. H. Davis, *J. Colloid Interface Sci.*, 1991, **144**, 412.
117 S. Okazaki, *Bull. Chem. Soc. Jpn.*, 1964, **37**, 144.
118 P. C. Duineveld, *J. Fluid Mech.*, 1995, **292**, 325.
119 M. Wu and M. Gharib, *Phys. Fluids*, 2002, **14**, L49.
120 S. A. K. Jeelani and S. Hartland, *J. Colloid Interface Sci.*, 1993, **156**, 467.
121 E. Klaseboer, Experimental and Numerical Study of Film Drainage Between Deformable Interfaces, PhD thesis, 1998.
122 O. D. Velev, G. N. Constantinides, D. G. Avraam, A. C. Payatakes and R. P. Borwankar, *J. Colloid Interface Sci.*, 1995, **175**, 68.
123 A. K. Chesters, *Trans. Inst. Chem. Eng.*, 1991, **69**, 259.

124 L. E. Scriven and C. V. Sternling, *Nature*, 1960, **187**, 186.
125 J.-P. Chevaillier, E. Klaseboer, O. Masbernat and C. Gourdon, *J. Colloid Interface Sci.*, 2006, **299**, 472.
126 E. Klaseboer, J. Ph. Chevaillier, A. Maté, O. Masbernat and C. Gourdon, *Phys. Fluids*, 2001, **13**, 45.
127 A. K. Chesters, *J. Fluid Mech.*, 1977, **81**, 609.
128 D. C. Bardos, *Surf. Sci.*, 2002, **517**, 157.
129 A. N. Zdravkov, G. W. M. Peters and H. E. H. Meijer, *J. Colloid Interface Sci.*, 2003, **266**, 195.
130 A. N. Zdravkov, G. W. M. Peters and H. E. H. Meijer, *J. Colloid Interface Sci.*, 2006, **296**, 86.
131 D. G. A. L. Aarts, H. N. W. Lekkerkerker, H. Guo, G. H. Wegdam and D. Bonn, *Phys. Rev. Lett.*, 2005, **95**, 164503.
132 D. G. A. L. Aarts and H. N. W. Lekkerkerker, *J. Fluid Mech.*, 2008, **606**, 275.
133 M. B. Nemer, X. Chen, D. H. Papadopoulos, J. Bławzdziewicz and M. Loewenberg, *Phys. Rev. Lett.*, 2004, **92**, 114501.
134 P. J. A. Janssen, P. D. Andersen, G. W. M. Peters and H. E. H. Meijer, *J. Fluid Mech.*, 2006, **567**, 65.
135 H. Lamb, *Hydrodynamics*, Cambridge University Press, 1932.

